

Master thesis and internship[BR]- Master's thesis : Reconstruction of Electropray Emitted Current using Computed Tomography[BR]- Internship

Auteur : Kazadi, Justine

Promoteur(s) : Hillewaert, Koen

Faculté : Faculté des Sciences appliquées

Diplôme : Master en ingénieur civil en aérospatiale, à finalité spécialisée en "aerospace engineering"

Année académique : 2023-2024

URI/URL : <http://hdl.handle.net/2268.2/20852>

Avertissement à l'attention des usagers :

Tous les documents placés en accès ouvert sur le site le site MatheO sont protégés par le droit d'auteur. Conformément aux principes énoncés par la "Budapest Open Access Initiative"(BOAI, 2002), l'utilisateur du site peut lire, télécharger, copier, transmettre, imprimer, chercher ou faire un lien vers le texte intégral de ces documents, les disséquer pour les indexer, s'en servir de données pour un logiciel, ou s'en servir à toute autre fin légale (ou prévue par la réglementation relative au droit d'auteur). Toute utilisation du document à des fins commerciales est strictement interdite.

Par ailleurs, l'utilisateur s'engage à respecter les droits moraux de l'auteur, principalement le droit à l'intégrité de l'oeuvre et le droit de paternité et ce dans toute utilisation que l'utilisateur entreprend. Ainsi, à titre d'exemple, lorsqu'il reproduira un document par extrait ou dans son intégralité, l'utilisateur citera de manière complète les sources telles que mentionnées ci-dessus. Toute utilisation non explicitement autorisée ci-avant (telle que par exemple, la modification du document ou son résumé) nécessite l'autorisation préalable et expresse des auteurs ou de leurs ayants droit.



Master thesis submitted to the Department of Aerospace and
Mechanical engineering of the University of Liège in partial
fulfillment of the requirements for the degree of Master in
Aerospace Engineering

Reconstruction of Electrospray Emitted Current using Computed Tomography

Author: Justine Kazadi
Thesis Supervisors: Prof. K. Hillewaert PhD. (ULiège)
D. Villegas-Prados (ienai SPACE)

UNIVERSITY OF LIÈGE
Faculty of Applied Sciences
Academic Year 2023-2024

ABSTRACT

This work aims to reconstruct the current emitted by an electrospray thruster using computed tomography, a technique that enables detailed, cross-sectional imaging of the emission pattern. Electrospray thrusters, known for their efficiency in space propulsion, require precise characterization of their emission profiles to optimize performance.

An experimental setup was developed featuring ATHENA, an electrospray thruster designed at IENAI SPACE, along with a tomography assembly that includes a wire collector and two motion stages: linear and rotary. This configuration allows for precise scanning of the thruster's emission profile.

To facilitate the reconstruction process, MATLAB codes were developed to simulate the emission patterns under various conditions. These simulations played a crucial role in visualizing expected outcomes and optimizing experimental parameters, such as the distance between the wire and the thruster, as well as the number of steps required for accurate data collection. Data was generated across voltage levels ranging from 700 V to 1300 V, which was used to create graphical representations of current intensity as a function of the stages' positions, known as sinograms. These sinograms were then processed using the inverse Radon transform to reconstruct the emission pattern as an image.

The resulting images aligned with the simulation predictions, and revealed non-uniform emission across the thruster. This non-uniformity, although expected due to manufacturing tolerances, provides valuable insights into the thruster's performance characteristics. The detailed analysis of these images suggests that certain regions of the thruster may require design modifications to improve emission uniformity.

ACKNOWLEDGMENTS

I would like to first thank Professor Koën Hillewaert for accepting to be my academic supervisor for the writing of my thesis.

I am also immensely grateful to the team at ienai SPACE for welcoming me so warmly during my internship. This experience provided me with a valuable glimpse into the working life within the space industry. I would like to extend a special thank you to David, my supervisor, for his guidance and availability, and to Borja, who always took the time to ensure I understood my tasks and knew how to proceed. I am also thankful to my fellow interns, who shared this experience with me and made it even more enriching.

I wish to thank my friend Lise for her help in reviewing my thesis. Your meticulous attention to detail greatly improved the quality of my work. Additionally, my heartfelt thanks go to Anastasia, whose companionship and support over the past two years have been invaluable, and also for reviewing my thesis.

Finally, I would like to express my deep appreciation to my family and friends for their unwavering support and encouragement throughout the entire duration of my studies. Your belief in me has been a constant source of motivation.

CONTENTS

1	Introduction	1
2	Literature Review	5
2.1	Principles of propulsion	5
2.1.1	Rocket equation and types of propulsion	5
2.1.2	Principles of electrospray	6
2.2	Radon Transform	12
2.2.1	Point source	13
2.2.2	Computed tomography	13
2.2.3	Inverse Radon transform	15
3	Experimental Set-up	19
3.1	Thruster	19
3.1.1	Emitter	20
3.1.2	Extractor	22
3.2	Tomography set-up	24
3.3	ARTEMIS	27
4	Analysis Methodology	29
4.1	Filtered backprojection	29
4.2	Simulations	32
4.2.1	Angular resolution	35
4.2.2	Linear resolution	39
4.2.3	Conclusion	43
5	Results	44
5.1	Multiple emitters	44
5.1.1	Sinogram	46
5.1.2	Backprojection	48
5.2	Discussion	49
6	Conclusion	50
A	Properties of the Radon Transform	52
A.1	Linearity	52
A.2	Symmetry	52
A.3	Scaling	52
A.4	Shifting	53

A.5	Rotation	53
A.6	Convolution	54
B	Delta Dirac function	55
	Bibliography	55

LIST OF FIGURES

1.1	ATHENA	4
2.1	Types of electrospray [1]	8
2.2	Externally wetted electrospray	9
2.3	Electrospray geometry	10
2.4	Emitter geometry	11
2.5	Variable change	12
2.6	Point source and its Radon transform	13
2.7	Illustration of the CT [2]	14
2.8	Attenuation coefficients	14
2.9	CT process [3]	16
2.10	Filtered backprojection process [4]	18
3.1	Thruster, exploded view	20
3.2	Nano-texturization of the cones	21
3.3	Feeding holes	21
3.4	Geometry for hydraulic impedance calculations	22
3.5	Extractor geometry	23
3.6	Stages	25
3.7	Set-up for tomography	26
4.1	Scanning method (angular step, linear sweep)	31
4.2	3D distribution	33
4.3	Plume divergence	34
4.4	Comparison of z_{probe}	35
4.5	Error between the ideal case and the reconstructed image as a function of the number of angular steps	37
4.6	Angular steps with a $z_{probe} = 0.5$ mm	38
4.7	Angular steps with a $z_{probe} = 1$ mm	39
4.8	Linear steps with a $z_{probe} = 0.5$ mm	41
4.9	Linear steps with a $z_{probe} = 1$ mm	42
5.1	Trapezoidal voltage	44
5.2	Current distribution for $\theta = 0$	45
5.3	Sinograms	47
5.4	Intensity maps	48

INTRODUCTION

Satellites have become essential in our daily lives. Beyond their well-known uses in telecommunications and broadcasting, they are also important for weather forecasting, Earth observation, military defense, and scientific research, including space exploration. As a result, CubeSats and microsattellites have rapidly become a significant part of the space industry. The small size of nanosatellites, which can be as compact as 10 cm and weigh around 10 kg, necessitates the miniaturization of all their components, including propulsion systems. However, miniaturizing traditional ion and Hall thrusters has proven difficult. These thrusters typically have larger dimensions that are not compatible with the limited size of nanosatellites. The primary challenge lies in power constraints, as these engines do not scale down efficiently in terms of power. When reduced in size, they suffer significant efficiency losses, making them less viable for smaller platforms. Additionally, these thrusters often require pressurized components, which add bulk and complexity, further complicating their integration into nanosatellites. [5] This is one of the reasons behind the interest of developing electrospray thrusters.

In the past, this technology has not been used often as spacecraft designers prefer to avoid risks and use well incorporated propulsion systems for these kind of missions. However, this trend is currently changing: the use of electric propulsion is growing in the industry. For instance, the satellite for the Lisa Pathfinder mission used electric propulsion, more specifically electrospray thrusters. Additionally, due to the increasing number of satellites in orbit, modern satellites need to be equipped with a specific system allowing its disposal at the end of its mission. Indeed, approximately 50% of satellites currently in orbit have been launched without any propulsion system. This lack of propulsion significantly complicates the process of de-orbiting and disposing of these satellites once they reach the end of their operational life. Without propulsion, these spacecraft are left to rely solely on atmospheric drag to gradually reduce their speed, causing them to eventually descend and burn up upon reentry into Earth's atmosphere. This passive method can take years or even decades, depending on the satellite's altitude and other factors, contributing to the growing issue of space debris.

As is displayed in TABLE 1.1, electrospray is adapted for a wide range of space maneuvers, including the ability to de-orbit satellites.

Mission type	VAT/PPT	Electrospray	Micro Gridded Ion Thruster
Exploration		x	x
Orbit\Inclination change		x	x
Attitude control	x	x	x
Station Keeping	x	x	x
Formation Flying	x	x	
Precision Attitude Control\Orbit Maintenance	x	x	
Spacecraft Detumble	x	x	x
De-orbit	x	x	x

Table 1.1: Electric thruster applicability to satellite mission type (VAT = Vacuum Arc Thruster, PPT = Pulsed Plasma Thruster) [6]

Electrospray propulsion is a type of electric propulsion that is particularly well-suited for CubeSats and microsattellites because of its compact size and its efficiency. This type of propulsion is based on the acceleration of charged particles contained in an Ionic Liquid (IL). This IL acts as a propellant.

The system is divided into two primary components: the extractor grid, which is grounded, and the emitter array, which is in direct contact with the liquid propellant. The voltage is applied to the ionic liquid through a metallic conductive reservoir. This action allows the creation of a potential difference, crucial for the electrospray process. The emitter array is in direct contact with the propellant liquid, consequently it is also being charged. This configuration is essential for creating the ionized plume that provides thrust in electrospray thrusters. The plume is a jet of finely atomized droplets created when the IL is subjected to an electric field. This field induces a charge on the liquid, causing it to break up into small particles and form a spray or plume.

If the potential created is sufficiently high, it will guide the particles to flow out of the system at high speed (around 20 km/s in the present case), creating thrust. [7] Different types of emitter arrays exist, but in this master thesis, the focus is on an externally wetted device consisting of a hundred and one micro-cones. These cones are designed to concentrate the electric field at their tips, enabling the emission of particles from those points. The array also includes feeding holes that facilitate the flow of ionic liquid from the reservoir to the cones, ensuring a continuous supply of propellant for the electrospray process.

Electrospray thrusters employ liquid propellant, more specifically ILs that do not require any pressurized tank or pressurized flow system as there is no necessity of keeping it under pressure compared to thermal propulsion thrusters (which is one of the main advantages of this type of propulsion system, the fact that this enables to have a smaller system).

A liquid with high conductivity is crucial for achieving high specific impulses in thrusters. Low volatility, on the other hand, is essential to minimize evaporation losses, especially in the vacuum of space. This property ensures that the liquid propellant remains stable and does not evaporate easily, eliminating the need for pressurized tanks, as previously mentioned. ILs possess both of these attributes and remain liquid at ambient temperature, making them an ideal choice for electrospray thrusters. ILs are chemically stable salts that melt at room temperature; however, they require careful handling due to their sensitivity to oxidation and humidity.

Formamide was considered for this type of application in the 2000s because it is an organic solvent with a wide range of attractive properties, such as a high dielectric constant and low volatility. However, it does have a non-negligible vapor pressure due to intermolecular Coulombic bonds. This vapor pressure is particularly problematic in space applications, where preventing evaporation is crucial, especially when the thruster is not in operation. If evaporation occurs, any residual liquid at the tip of the thruster could evaporate, potentially leaving behind salts. These salts could then obstruct the tip, leading to blockages that would hinder the thruster's ability to restart. This is why it has largely fallen out of use and has been replaced by ILs. [8]

Given the critical need for precise and reliable performance in electrospray thrusters, it becomes essential to thoroughly characterize their emission profiles. Electrospray thrusters can exhibit non-uniform emission profiles along the cones, leading to variations in performance. Additionally, understanding off-axis emission sites is vital as they may impact the overall thrust vector and efficiency. Another significant concern is the potential for particles to impact the extractor grid, which could lead to short-circuiting and damage to the thruster system. These challenges necessitate a detailed analysis of the emission characteristics, and this is where tomography becomes helpful.

By offering the ability to produce detailed cross-sectional images, tomography allows for a comprehensive analysis of the thruster's emission patterns. This advanced imaging technique, commonly used in medical applications, is adapted in this thesis to focus on the current emitted by the thruster, providing a clear picture of its operational performance. What is analyzed here is the current emitted by the thruster instead of the intensity variation of X-Rays. The results of computed tomography (CT) can be visualized using a sinogram.

This graphical representation displays the varying intensity of the current, with the color spectrum ranging from maximum values, typically shown in white, to minimum values, represented in black. The axes are the radial and angular positions of the instrument used, a wire. The graph can be read in the following manner: each point corresponds to a current intensity for a given linear position as well a angle [9] at which the wire is positioned during the gathering of data. With a sinogram one thus has all the information necessary to do a reconstruction of the current profile, and consequently the emission of the thruster which is the object of the present work.

The purpose of this thesis is the analysis of the current emission of a thruster, in order to find out as precisely as possible which of the hundred and one cones are emitting and observe the variation of the emission with time as well. In order to so, the exhaustive performance study is using computed tomography. The thruster employed here is being developed by ienai SPACE, ATHENA (Adaptable THRuster based on Electrospray powered by NANotechnology) and is showed in FIGURE 3.1. [10]



Figure 1.1: ATHENA

The structure of this thesis is as follows: The second chapter provides a literature review, covering the experimental background needed to understand the thesis. The third chapter details the experimental setup, including the steps taken for analysis. The fourth chapter describes the methodology used to interpret the data collected from the experiments. Finally, the last chapter presents a thorough explanation of the results and their analysis.

LITERATURE REVIEW

In order to allow the reading of this thesis to be as smooth as possible, this chapter is dedicated to the display of the theory required for the understanding of the concepts used throughout this whole work.

2.1 Principles of propulsion

2.1.1 Rocket equation and types of propulsion

Propulsion is based on EQUATION 2.1, the rocket equation, where ΔV corresponds to the change in velocity, the exhaust velocity is $v_e = gI_{sp}$ with g the gravity constant and I_{sp} the specific impulse, m_0 the initial mass, and m_f the final mass of the spacecraft.

The ΔV budget is found by adding the multiple changes in velocity during the spacecraft's entire mission, it is usually associated with orbital maneuvers, or to counteract space effects such as solar pressure, J_2 effects linked to the oblateness of Earth, and atmospheric drag.

$$\Delta V = v_e \ln\left(\frac{m_0}{m_f}\right) = gI_{sp} \ln\left(\frac{m_0}{m_f}\right) \quad (2.1)$$

Looking at EQUATION 2.1, one can understand the importance of specific impulse: the higher I_{sp} , the more velocity changes are allowed. This suggests that the specific impulse needs to be maximized. However, it is important to keep in mind that while achieving a higher specific impulse results in more efficient maneuvering by reducing the amount of propellant needed, it also requires more time to execute maneuvers.

Propulsion systems can be divided into two categories: thermal and electric propulsion. They differ in terms of specific impulse and generated thrust. Indeed, thermal systems usually have an I_{sp} varying between 200 s and 500 s and generate thrust in the order of millions of Newtons. This makes them most adequate for launchers. On the other hand, the specific impulse of electric propulsion systems can go up to thousand of seconds, but they cannot produce thrust higher than millinewtons. This makes them more suited for on-orbit maneuvers that require the assistance of propulsion. This highlights the attractiveness of

electric propulsion: the higher I_{sp} allows for a higher ΔV .

2.1.2 Principles of electrospray

EQUATION 2.2 shows the basic principle on which electric propulsion is based: the acceleration of emitted particles with the help of an electric potential. m is the mass of a single particle, its velocity is c and charge q , and V is the voltage that accelerates the particle.

$$\frac{1}{2}mc^2 = qV \quad (2.2)$$

Electrospray is a type of electric propulsion and consists of emitted particles accelerated by an electric potential that is formed between an IL (the propellant) and a grid, which leads to the formation of a momentum flux.

This configuration can lead to the formation of a Taylor cone. Indeed, the interface between an IL and vacuum is a junction between a conducting fluid and a dielectric. The presence of an electric field induces a destabilization of that liquid surface, resulting in the formation of a cone (the so-called Taylor cone). However, this is only possible if a threshold is reached.[11]

As soon as a voltage threshold is reached, a spray containing particles is created. This is shown by RELATION 2.3, where R_c is the radius of curvature of the cone tip, γ is the liquid surface tension, ϵ_0 is the vacuum permittivity, and E_{tip} the electric field at the tip of the cone.

$$\frac{1}{2}\epsilon_0 E_{tip}^2 > \frac{2\gamma}{R_c} \quad (2.3)$$

Particles are ejected from the Taylor cone as soon as RELATION 2.3 is verified, the latter represents the electric pressure (surface traction due to electric field) being larger than the effective capillary pressure at the tip of a cone.

The thrust is evaluated with EQUATION 2.4, where I_T is the emitted current beam, V_b the beam potential, $\frac{q}{m}$ the charge-to-mass ratio of the particles, and \dot{m} the mass flow rate of the ionic liquid.

$$T = I_T \sqrt{2V_b \frac{m}{q}} \quad (2.4)$$

The numerical value of the thrust can be determined by recognizing that the ratio of charge to mass, $\frac{q}{m}$, remains constant for each ion. Consequently, the time derivative of this ratio is zero, which leads to EQUATION 2.5. From this equation, it becomes evident that $\dot{m}q = m\dot{q}$. Considering that the electric current is given by $I = \frac{dq}{dt}$, the mass flow rate

expression can be derived, resulting in EQUATION 2.6.

$$\frac{d}{dt}\left(\frac{m}{q}\right) = \frac{\dot{m}q - m\dot{q}}{q^2} = 0 \quad (2.5)$$

$$\dot{m} = I \frac{m}{q} \quad (2.6)$$

The specific impulse is computed with EQUATION 2.7.

$$I_{sp} = \frac{T}{\dot{m}g} = \frac{1}{g} \sqrt{2V_b \frac{q}{m}} \quad (2.7)$$

Since the emission site consists of an array of individual emission points, the total thrust can be calculated by summing the contributions from each individual cone. This approach allows the overall thrust to be determined by aggregating the effects of all cones, while maintaining the specific impulse. This method of calculation is advantageous because it enables a detailed analysis of thrust distribution across the array, ensuring that the specific impulse remains consistent across different operational conditions.

EQUATION 2.8 allows to quantify the propulsive efficiency [12]. It is the ratio of the useful kinetic energy that produces thrust to the total energy expended by the propulsion system.

$$\eta = \frac{T^2}{2\dot{m}V_0 I} \quad (2.8)$$

Propulsive efficiency is crucial for understanding the optimization of propulsion systems for fuel efficiency and performance. Higher propulsive efficiency leads to a better fuel consumption, which is vital for long missions.

The electrospray is divided into two main parts: the emitter and the grid. The emitter is the part of the system where the ionic liquid is exposed to the electric field, ultimately generating thrust. The grid on the other hand will generate the electric field in itself. Both parts have their own specificities that will be further described in the remainder of this section.

Types of emitters for electrospray

The emitter can be supplied using various methods, with three main types shown on FIGURE 2.1. The first one being used here is externally wetted, where it is the surface that is actually being wetted by the propellant. The difference with the other two methods is that the propellant comes from within the emitter. Indeed, the second is called porous because it requires a porous material where the propellant is brought which allows the feeding of

the emitter by capillarity. The last method is named internally fed, the liquid is put in a container before being brought to the emission site with the help of pressure control.

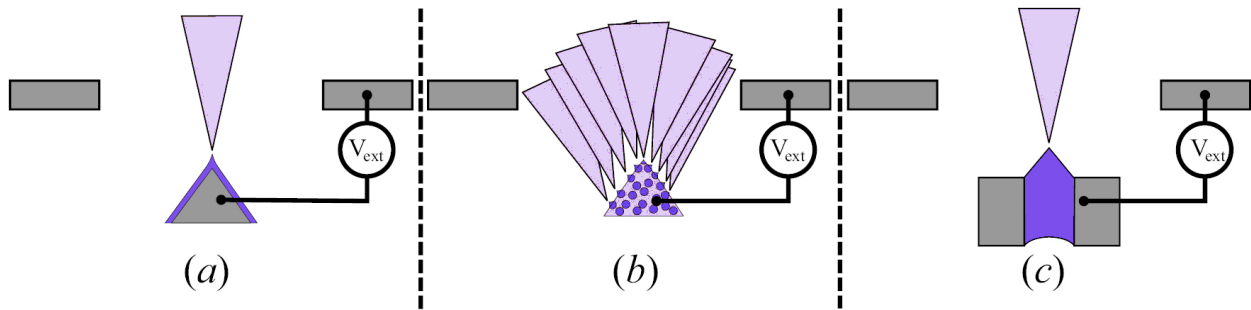


Figure 2.1: Types of electro spray [1]

This master thesis focuses solely on externally wetted emitters. FIGURE 2.2 is an illustration of how this specific electro spray works in detail. The emitter is a tip covered in ionic liquid, but this liquid cannot be simply added on its surface. Instead, electrowetting is used: the liquid moves upward only once a potential is applied and the latter has reached a threshold that corresponds to the emission voltage. When the liquid has arrived at the top of the emitter and the electric field continues to increase, the liquid deforms into a Taylor cone. This leads to field enhancement that generates high local electric field which allows the cone to continue its deformation into a cone jet, that will become a droplet emission, pure ions emission or ideally produces a mixture of both. As soon as there is a high enough electric field, the ions are able to leave the interface formed by the liquid. [13] These thrusters are adaptable because of the possibility to have a multitude of Taylor cones. [14]

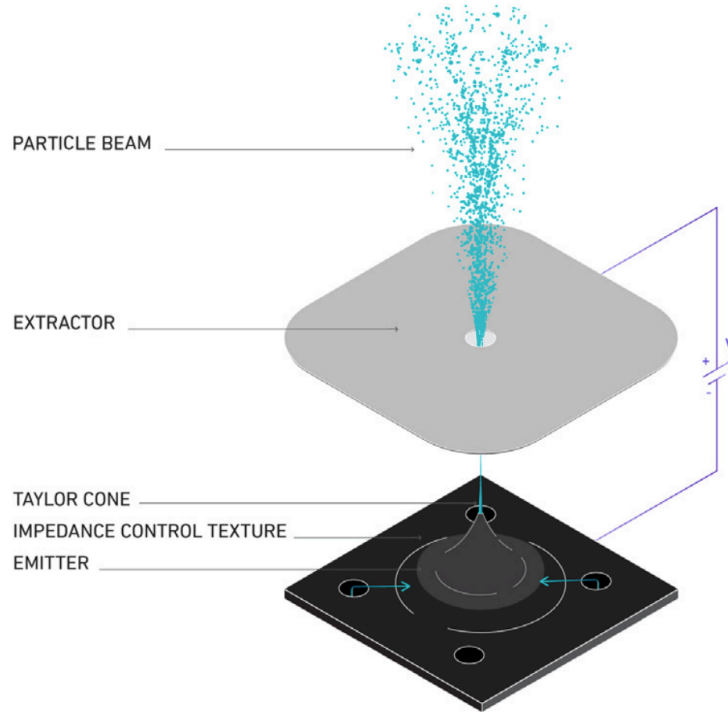


Figure 2.2: Externally wetted electrospray

Intensity of the electric field

The thrust is generated by applying an electric field on the ionic liquid. This electric field is generated by applying a potential difference between the emitter and the grid.

The shape of the applied electric field is primarily determined by the geometry of the emitter, the design of the extractor - which facilitates the potential difference - and the spacer that is the area between the emitter and extractor. The intensity of this field is governed by the applied potential difference. Both the characteristics of the emission and the efficiency of particle interception are influenced by the propellant flow and the electric field established between the extractor and emitter.

The significance of the emitter-extractor geometry lies in its direct influence on the shape of the electric field and the strength at the tip, which are critical not only for the emission process but also for controlling beam divergence. To prevent excessive impact on the extractor, the emitter-extractor half-angle must be carefully designed to exceed the expected main beam half-angle. This consideration is crucial in ensuring efficient propulsion performance and minimizing losses.

EQUATION 2.9 defines the tip-to-extractor distance, in cylindrical coordinates.

$$dz = h_s - t_e - h_c \quad (2.9)$$

h_s is the spacer height, t_e the thickness of the emitter base, and h_c the height of emitter's cones. The radial component can be expressed as $dr = \frac{Dx}{2}$, where Dx represents the diameter of the extractor holes. These dimensions are presented on FIGURE 2.3. Two other crucial parameters that must be defined are the tip-to-base side distance, denoted as d , and the half-angle α . These parameters are defined as follows:

$$d = \sqrt{dz^2 + dr^2}, \quad (2.10)$$

$$\alpha = \arctan\left(\frac{dr}{dz}\right). \quad (2.11)$$

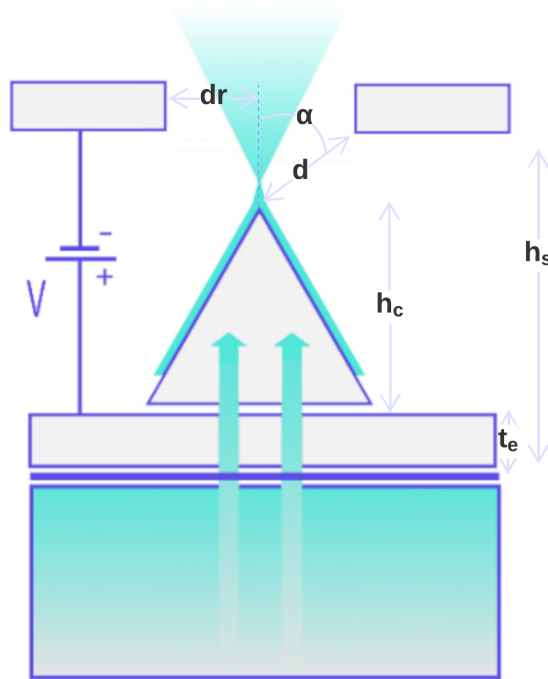


Figure 2.3: Electro spray geometry

The emitted current is independent of the height of the cones. The tip geometry plays a more crucial role than the overall size of the cone. This lack of dependence on cone size is one of the driving factors behind the trend toward miniaturization in this technology. By reducing the size of the cones, it is possible to achieve higher emitter densities without compromising the performance, making the technology more efficient and adaptable for various applications, particularly in the context of space propulsion systems of small satellites.

The emitter density, \tilde{N} , can be computed using EQUATION 2.12, where A is the effective emitter area and d_c the distance between two cones as illustrated on FIGURE 2.4.

$$\tilde{N} = \frac{1}{A} = \frac{2}{d_c^2 \sqrt{3}} \quad (2.12)$$

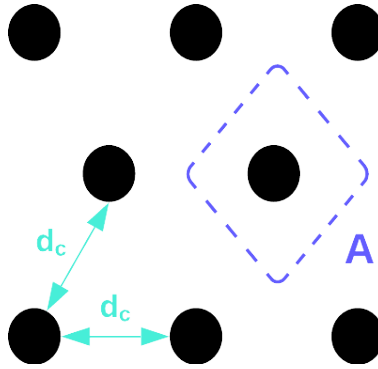


Figure 2.4: Emitter geometry

To enable a sufficient amount of current to be emitted from the cone tips, a minimum voltage, V_s , must be applied. This voltage can be estimated based on the geometry of the cone. It is determined using EQUATION 2.13, where G represents the distance between the tips of the cones and the extractor, and R_c is the radius of the emitter tip. It is important to note that for this assessment, the condition $2G \gg R_c$ should be met, indicating that the distance between the emitter and extractor is significantly larger than the emitter tip radius. This relationship helps ensure that the electric field is strong enough to facilitate the desired emission of current from the cone tips. [15][16]

$$V_s = \sqrt{\frac{\gamma R_c}{\epsilon_0}} \ln\left(\frac{2G}{R_c}\right) \quad (2.13)$$

Additionally, it is important to consider the possibility that some particles could reach the surface underneath the extractor plate, a scenario that must be avoided to maintain efficient operation and risks of short-circuiting. As electro spray thrusters evolve toward smaller emitter sizes, it becomes increasingly important to position the grid closer to the emitter. This closer proximity helps reduce the risk of beam merging before the beams pass through the grid, which is vital for maintaining a clear and distinct emission profile.

Failing to adjust the grid-emitter distance appropriately could lead to several undesirable outcomes. One significant issue is the potential need for higher voltages to maintain the same tip field strength, as particles that collide with the extractor are lost and do not contribute to thrust. This not only complicates the system design but also increases the risk of operational inefficiencies and potential damage to the thruster. Therefore, careful consideration of the grid placement relative to the emitter size is essential to optimize performance and ensure the longevity of the thruster.

2.2 Radon Transform

The foundation for evaluating the current density in this work is based on the Radon transform. The general expression for the linear Radon transform is given in EQUATION 2.14. However, for the purposes of this study, a two-degree-of-freedom expression is needed, whereas the general form contains three degrees of freedom. In order to resolve this issue, the solution is to make use of a variable change.

This adjustment involves defining a line that corresponds to the collecting instrument, which is a wire. The equation describing this line is $\rho = x \cos \theta + y \sin \theta$. In other terms, the coordinates can be expressed as $(\xi_0, \xi_1, \xi_2) = (\rho, \cos \theta, \sin \theta)$. FIGURE 2.5 illustrates this line and its associated parameters, where θ represents the rotation of the line and ρ signifies the shortest distance from the origin to the line. This variable change simplifies the Radon transform to a form that aligns with the experimental setup, enabling more accurate analysis of the current density along the wire. [2]

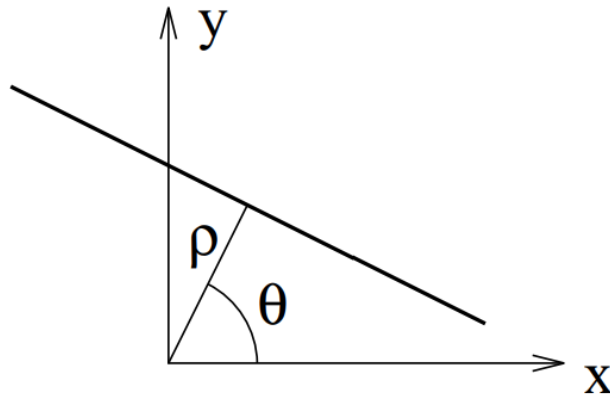


Figure 2.5: Variable change

$$\tilde{g}(\xi_0, \xi_1, \xi_2) = \int_{-\infty}^{\infty} \int_{-\infty}^{\infty} g(x, y) \delta(\xi_0 - \xi_1 x - \xi_2 y) dx dy \quad (2.14)$$

This allows to obtain a more adequate version of the Radon transform as EQUATION 2.15, which is commonly used for computed tomography or even astronomy. This transform has some interesting properties that are displayed in APPENDIX A.

$$\tilde{g}(\rho, \theta) = \int_{-\infty}^{\infty} \int_{-\infty}^{\infty} g(x, y) \delta(\rho - x \cos \theta - y \sin \theta) dx dy \quad (2.15)$$

With δ the Dirac delta function, and \tilde{g} the Radon transform of a continuous two dimensions function g .

From the definition of the Dirac delta function (APPENDIX B), which is

$$\delta(x) = 0 \quad \text{for } x \neq 0, \quad (2.16)$$

one can find an equivalent to the previous expression, which will be useful later for the computed tomography,

$$\tilde{g}(\rho, \theta) = \int_{-\infty}^{\infty} g(\rho \cos \theta - s \sin \theta, \rho \sin \theta + s \cos \theta) ds. \quad (2.17)$$

2.2.1 Point source

To gain a deeper understanding of the results of the Radon transform, the analysis begins with a point source located at coordinates (x_0, y_0) . This point serves as a simple yet fundamental case for evaluating the transform's behavior.

The arbitrary g function is defined as follows:

$$g(x, y) = \delta(x - x_0)\delta(y - y_0), \quad (2.18)$$

which in result brings the Radon transform to be

$$\tilde{g}(x, y) = \int_{-\infty}^{\infty} \int_{-\infty}^{\infty} \delta(x - x_0)\delta(y - y_0)\delta(\rho - x \cos \theta - y \sin \theta) dx dy \quad (2.19)$$

$$= \delta(\rho - x_0 \cos \theta - y_0 \sin \theta). \quad (2.20)$$

As shown in FIGURE 2.6, the Radon transform of a point results in a sinusoid.

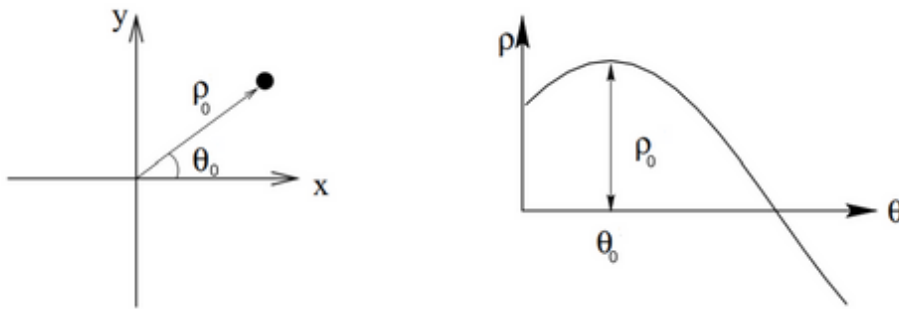


Figure 2.6: Point source and its Radon transform

2.2.2 Computed tomography

The typical CT scanner works with X-rays, where an object is analyzed by looking at the variation in intensity of rays after going through the object in question. As the rays are

assumed to move following a straight line, each emitted ray is collected by a detector directly on the other side of the body, this process is illustrated on FIGURE 2.7.

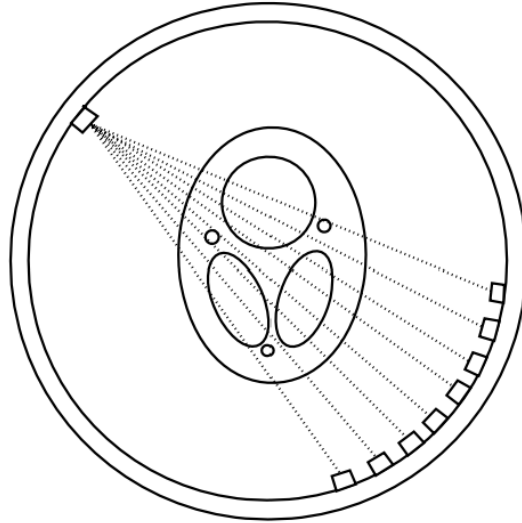


Figure 2.7: Illustration of the CT [2]

The parameter of interest is the intensity change, thus one can define μ to be the attenuation coefficient. As for the lines followed by the rays, they are parameterized with (ρ, θ) as was previously discussed.

On account of the non-homogeneity of the studied object, one can assume that the rays will encounter different attenuation coefficients during their journey. An illustration of this process can be observed on FIGURE 2.8.

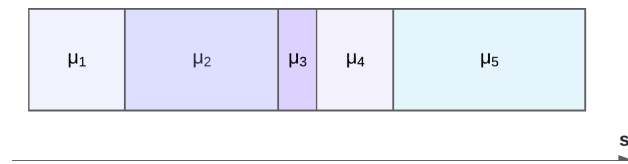


Figure 2.8: Attenuation coefficients

In order to represent this, the intensity can be expressed with EQUATION 2.21, where I_0 corresponds to the emitter's own intensity, and s_i is the coordinate along the s-axis.

$$I(\rho, \theta) = I_0 e^{-\sum_i \mu_i s_i} \quad (2.21)$$

When generalizing the expression, with the assumption that μ is a function of s, one can adjust the equation to

$$I(\rho, \theta) = I_0 e^{-\int \mu(x,y) ds}. \quad (2.22)$$

From this, the projection can be defined as follows

$$P(\rho, \theta) = \log\left(\frac{I_0}{I(\rho, \theta)}\right) \quad (2.23)$$

$$= \int_{-\infty}^{\infty} \mu(x, y) ds \quad (2.24)$$

$$= \int_{-\infty}^{\infty} \mu(\rho \cos\theta - s \sin\theta, \rho \sin\theta + s \cos\theta) ds. \quad (2.25)$$

Examining this projection more closely, it becomes evident that it represents the Radon transform, as defined by EQUATION 2.17, of the intensity factor. Consequently, this result can be rearranged to

$$P(x, y) = \int_{-\infty}^{\infty} \int_{-\infty}^{\infty} \mu(x, y) \delta(\rho - x \cos\theta - y \sin\theta) dx dy. \quad (2.26)$$

One can thus conclude that to obtain the intensity variation, the inverse Radon transform must be applied. The details of this process are the focus of the following section.

2.2.3 Inverse Radon transform

There exist multiple methods to generate the inverse Radon transform, however only one will be employed here, namely the backprojection. In addition one can use a filter to allow the reconstructed image to be more accurate. The difference between the two possibilities can be observed on FIGURE 2.9. This particular image is a mathematical phantom, typically used to verify algorithms built for image reconstruction. It represents the human head because CT's first use is in medical imaging. The variation of the gray color observed is explained by the variation of density. [17]

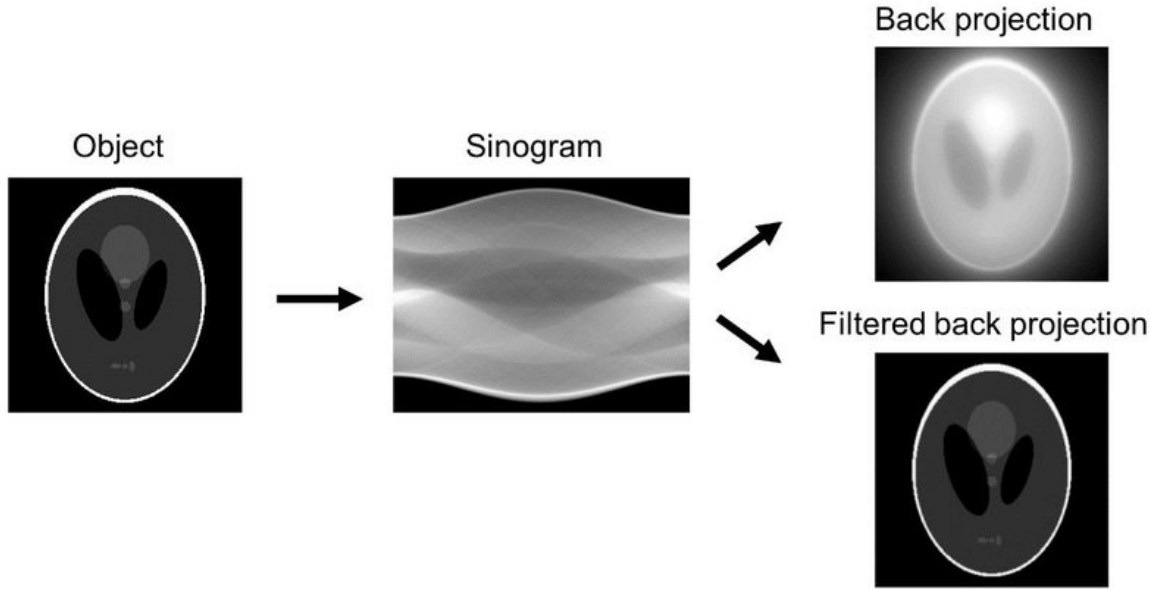


Figure 2.9: CT process [3]

In order to compute the inverse Radon transform of \tilde{g} , it is necessary to first express the Fourier transform of the function g . This development is carried out through EQUATION 2.27.

$$G(k_x, k_y) = \int_{-\infty}^{\infty} \int_{-\infty}^{\infty} g(x, y) e^{-i2\pi(k_x x + k_y y)} dx dy \quad (2.27)$$

From this 2D Fourier transform, the inverse Radon transform can be found following EQUATION 2.28.

$$g(x, y) = \int_{-\infty}^{\infty} \int_{-\infty}^{\infty} G(k_x, k_y) e^{i2\pi(k_x x + k_y y)} dk_x dk_y \quad (2.28)$$

The filtered backprojection is obtained using the following equations, after transforming the coordinates to polar coordinates.

$$\begin{aligned} k_x &= \nu \cos\theta \\ k_y &= \nu \sin\theta \end{aligned}$$

$$g(x, y) = \int_0^{2\pi} \int_0^{\infty} \nu G(\nu \cos \theta, \nu \sin \theta) e^{i2\pi\nu(x \cos \theta + y \sin \theta)} d\nu d\theta \quad (2.29)$$

$$= \int_0^{\pi} \int_{-\infty}^{\infty} H(\nu) G(\nu \cos \theta, \nu \sin \theta) e^{i2\pi\nu(x \cos \theta + y \sin \theta)} d\nu d\theta \quad (2.30)$$

$$= \int_0^{\pi} \int_{-\infty}^{\infty} H(\nu) \left(\int_{-\infty}^{\infty} \tilde{g}(\tilde{\rho}, \theta) e^{-i2\pi\tilde{\rho}\nu} d\tilde{\rho} \right) e^{i2\pi\nu(x \cos \theta + y \sin \theta)} d\nu d\theta \quad (2.31)$$

From these, two distinct components can be identified. The first component corresponds to the filtering stage, while the second involves the integration. The integration over a sine curve functions serves as the backprojection, reconstructing the image from the projections. Meanwhile, the filtering is performed using a high-pass filter, specifically $H(\nu)$, to enhance the image by eliminating low-frequency noise and sharpening the details.

$$\bar{\tilde{g}}(\rho, \theta) = \int_{-\infty}^{\infty} H(\nu) \left(\int_{-\infty}^{\infty} e^{-i2\pi\tilde{\rho}\nu} d\tilde{\rho} \right) e^{i2\pi\rho\nu} d\nu \quad (2.32)$$

$$= IFT_{\nu \rightarrow \rho} \{ H(\nu) FT_{\tilde{\nu} \rightarrow \rho} \{ \tilde{g}(\tilde{\rho}, \theta) \} \} \quad (2.33)$$

The last step of the procedure is executed with EQUATION 2.35, where the function g is finally recovered.

$$g(x, y) = \int_0^{\pi} \bar{\tilde{g}}(x \cos(\theta) + y \sin(\theta), \theta) d\theta \quad (2.34)$$

$$= \int_0^{\pi} \int_{-\infty}^{\infty} \bar{\tilde{g}}(\rho, \theta) \delta(\rho - x \cos \theta - y \sin \theta) d\rho d\theta \quad (2.35)$$

To enable the filtering process, the following filter is applied, where \star denotes the convolution product.

$$H(\nu) = \frac{-i \operatorname{sign}(\nu)}{2\pi} i2\pi\nu \quad (2.36)$$

$$\Rightarrow \bar{\tilde{g}}(\rho, \theta) = IFT_{\nu \rightarrow \rho} \left\{ \frac{-i \operatorname{sign}(\nu)}{2\pi} i2\pi\nu FT_{\tilde{\nu} \rightarrow \rho} \{ \tilde{g}(\tilde{\rho}, \theta) \} \right\} \quad (2.37)$$

$$= \frac{1}{2\pi^2\rho} \star \frac{\partial \tilde{g}(\rho, \theta)}{\partial \rho} \quad (2.38)$$

The method detailed here is summarized in FIGURE 2.10.

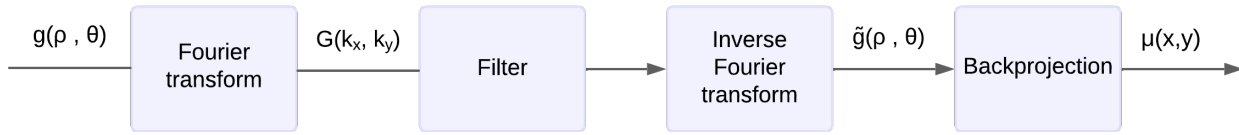


Figure 2.10: Filtered backprojection process [4]

The Shepp-Logan filter is a *sinc* window that is multiplied by the ramp filter in order to improve the signal to noise ratio. The expression of this filter is as follows:

$$H(\nu)_{Shepp-Logan} = H(\nu) \frac{\sin(\frac{\pi\nu}{2\nu_l})}{2\frac{\pi\nu}{2\nu_l}}, \quad (2.39)$$

with $\nu_u = \frac{1}{2\Delta}$, the upper limit corresponding to the Nyquist criterion and Δ being the distance between detectors. Indeed, the Nyquist criterion states that the frequency should not be higher than half of the sampling frequency. ν_l is the lower limit. Both limits are noting that if $\nu_l < H(\nu) < \nu_u$ the filter will be zero.

Another important criterion to ensure accurate signal identification is to meet a minimum number of angles, which ensures sufficient angular sampling. This requirement can be expressed mathematically as EQUATION 2.40, where m represents the number of angles and n denotes the number of data points per angle. It is crucial that these m angles are evenly distributed over an angular range of at least 180 degrees. Failure to meet this sampling criterion can lead to distortions or inaccuracies in the reconstructed image, as insufficient angular coverage may result in misrepresentations of the object's structure. [18]

$$m > \frac{\pi}{2}n \quad (2.40)$$

EXPERIMENTAL SET-UP

3.1 Thruster

ATHENA, an electrospray thruster developed by ienai SPACE, is used in the present work. ATHENA is an adaptable thruster, allowing the number of emitters to be variable and adjusted based on specific requirements. In this study, a single emitter array comprising a hundred and one micro-cones is used. This emitter array is externally wetted and paired with an extractor grid, with the grid's holes precisely aligned with the positions of the cones on the emitter. The separation distance between the grid and the emitter is determined based on various parameters, as discussed in SECTION 2.1.2.

FIGURE 3.1 shows an exploded view of the thruster. One can observe the different parts that compose the thruster, namely the extractor, emitter, the PCB (Printed Circuit Board) that is required to induce the voltage, propellant reservoir, and the mounting screws that can also serve as connectors.

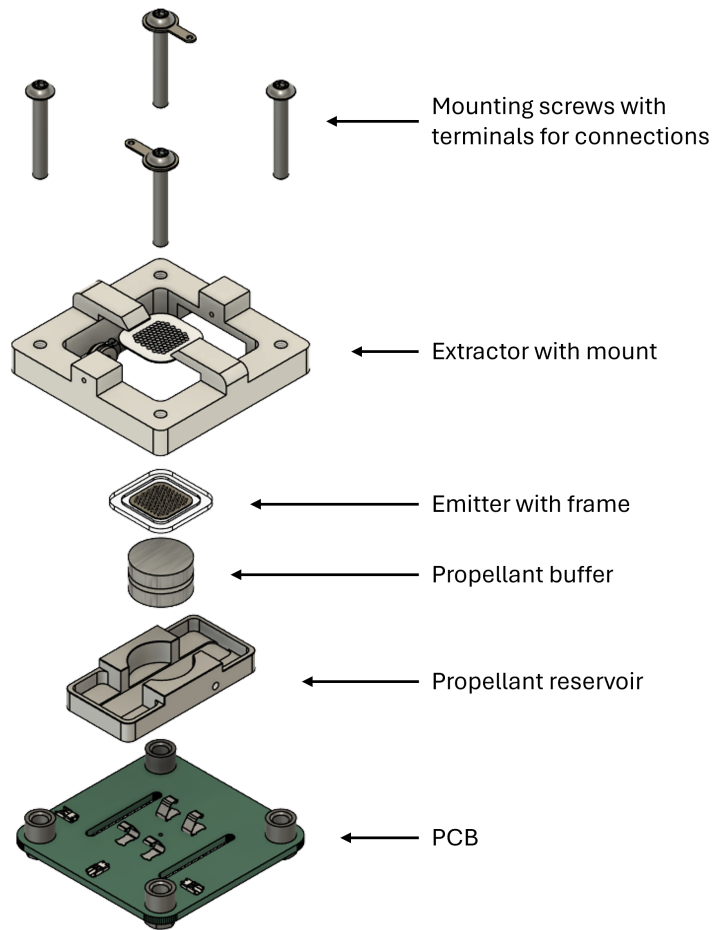


Figure 3.1: Thruster, exploded view

3.1.1 Emitter

To optimize the design of the emitter array, several key considerations are addressed. These include the hydraulic impedance, which is crucial for ion emission; the structural integrity of the electrospray array, ensuring it withstands electrostatic loads without breaking; and the geometry that minimizes the starting voltage, as discussed in SECTION 2.1.2. Additionally, the final assembly must prevent any liquid leakage and ensure that the ion beam is not intercepted by any surface. [16]

To facilitate the flow of liquid propellant to the emitter tips while controlling hydraulic impedance, the cones are nano-texturized, as shown in FIGURE 3.2. The emitter is also designed with small feeding holes, visible in FIGURE 3.3, which allow the liquid to flow from the reservoir to the emitter tips. These holes are shaped like small stars to optimize liquid distribution.

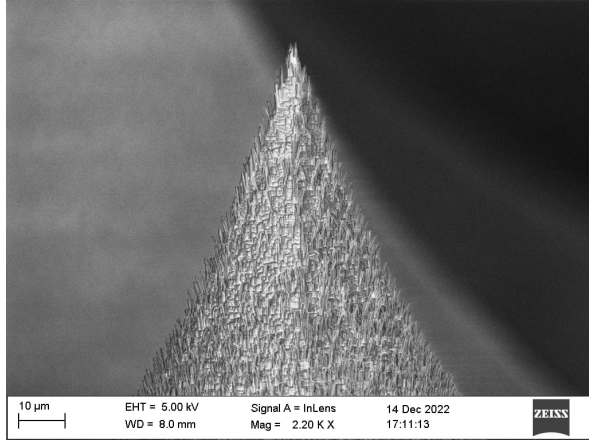


Figure 3.2: Nano-texturization of the cones

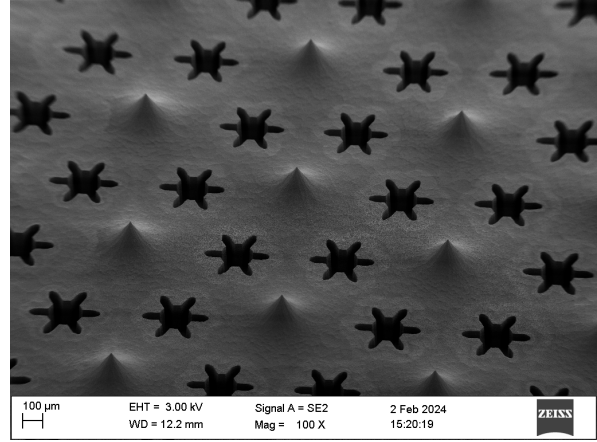


Figure 3.3: Feeding holes

The emitters require high hydraulic impedance, which can be evaluated by making an analogy with a flow inside an open capillary. One can thus make use of Darcy's law,

$$\vec{q}_s = -\frac{K_{ps}}{\mu} \vec{\nabla} P, \quad (3.1)$$

with q_s the volumetric surface flow rate flux, K_{ps} the surface permeability, μ the fluid's viscosity, and P the pressure. The variation of pressure is calculated based on the geometry of the cone, with the references illustrated on FIGURE 3.4, where one can see the motion of the fluid, flowing from z_2 to z_1

$$\Delta P = -\frac{\mu}{K_{ps}} \int_{z_1}^{z_2} \frac{Q}{2\pi z \sin\theta} dz \quad (3.2)$$

$$= \frac{\mu Q \ln\left(\frac{z_1}{z_2}\right)}{2\pi K_{ps} \sin\theta}. \quad (3.3)$$

The flow rate, Q , is computed as follows, with the current I , the average molar mass of emitted particles $\langle M \rangle$, the Avogadro number N_{AV} , the elementary charge e , and the liquid's density ρ ,

$$Q = \frac{I \langle M \rangle}{N_{AV} e \rho}. \quad (3.4)$$

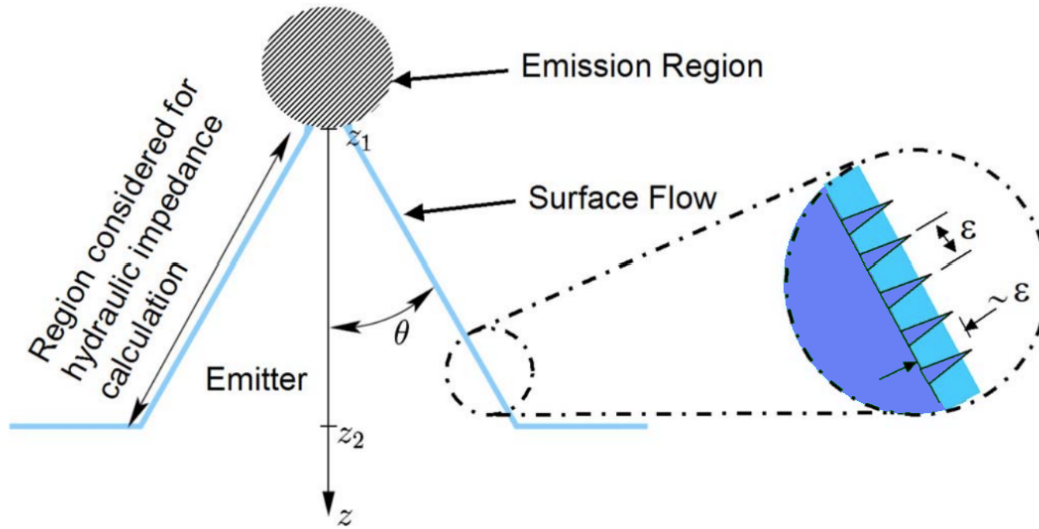


Figure 3.4: Geometry for hydraulic impedance calculations

3.1.2 Extractor

The objective of the extractor is to facilitate the extraction of particles from the emitter by applying a voltage. The design of the extractor is crucial to achieve optimal performance, characterized by high emitter density and low extraction voltage. High density refers to the number of cones per unit area, which necessitates placing the holes in the extractor as close together as possible. This requires minimizing the distance between the holes while still maintaining the structural integrity of the extractor.

FIGURE 3.5 displays the geometry of the extractor and convention used. From those parameters one can write a condition for the beam to avoid being intercepted by the extractor

$$\frac{a-b}{2h} > \tan\theta_{beam}, \quad (3.5)$$

as well as the expression of the distance between the emitter and extractor, G ,

$$G = \sqrt{\frac{(a-b)^2}{4} + (h-H)^2}. \quad (3.6)$$

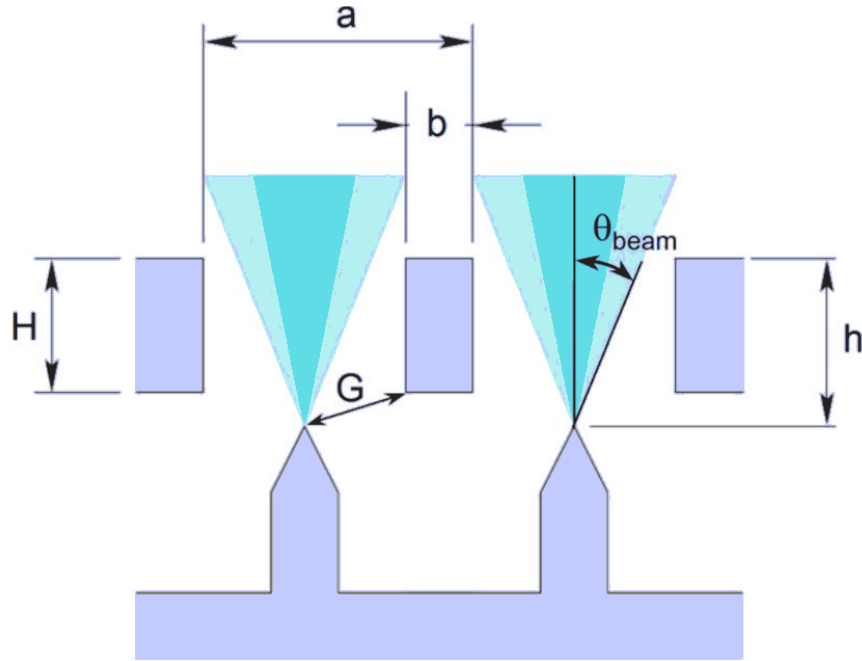


Figure 3.5: Extractor geometry

In designing the extractor, it is essential to consider the electrostatic forces that can generate a load on the extractor, potentially causing it to move closer to the emitter, a reaction that must be avoided. Two critical effects are analyzed here: the electrostatic pressure and the resulting deflection. These are calculated as follows;

$$P_{el} = \frac{\epsilon_0 V^2}{2d^2}, \quad (3.7)$$

$$\delta = \frac{P_L L^4}{32EH^3b}. \quad (3.8)$$

d is the value equivalent to the distance between two capacitors with the assumption that the extractor acts as parallel plates capacitor.

It can be postulated that the extractor is composed of multiple structural beams arranged in a row, each with a rectangular cross-section defined by the dimensions b (width) and H (height), as illustrated in FIGURE 3.5. The length of the beam is denoted by L . The uniform pressure acting on the beam is represented by P_L , and E is the Young's modulus of the material. [19] [16]

With the help of the equivalence between the extractor and structural beams, the problem can be solved by using $P_L = \frac{a}{b}P_{el}$, and stating that d 's value is close to $h - H$. This leads to

$$\delta = \frac{\epsilon_0 V^2 L^4 a}{64(h-H)^2 E H^3 b^2} \quad (3.9)$$

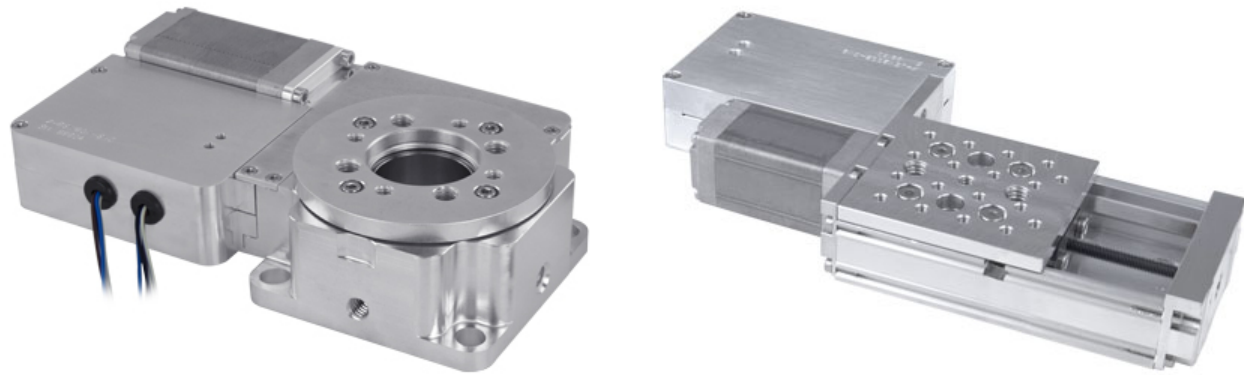
Finally, the maximum bending stress can be evaluated with

$$\sigma = \frac{P_L L^2}{2H^2} = \frac{a\epsilon_0 V^2 L^2}{4b(h-H)^2 H^2}. \quad (3.10)$$

3.2 Tomography set-up

The tomography is executed with the help a system made of a linear translation stage that allows the sweeping of a wire through the plume of the electrospray which thus enables the collection of the current. This action is equivalent to doing an integration of the current density multiplied by the thickness of the wire. The set-up is also equipped with a rotational stage which allows sweeping for different configurations. FIGURE 3.7 displays the schematic set-up of the rotary stage on the left and the linear stage on the right. The combination of radial and angular positions changes for each measurement allowing an extensive collection of data. The latter can then be used to create a 2D current map and current density distribution. [20]

Both stages are manufactured by the Canadian company Zaber. Their control is possible with a serial connection and the "Zaber_motion" library in Python language. The Zaber rotary stage is perfectly built for vacuum as it is made of materials that minimize outgassing, it allows up to a 360° range, has only one axis and is assorted with a controller. Furthermore, it provides a torque up to 100 N · cm and has a load capacity of 20 kg. [21] The Zaber X-LSM-SV2 is a high vacuum, miniature, motorized linear stage with a built-in controller. It has a resolution of 20 μm, can support up to 10 kg of centered load and 300 N · cm of cantilever load. Identically to the rotary stage, it is made of vacuum compatible materials and is vacuum compatible as low as 10e⁻⁶ Torr. Both stages also support standard serial connection [22], their pictures are shown on FIGURE 3.6.



(a) Rotary

(b) Linear

Figure 3.6: Stages

The thruster is mounted on the set-up with careful attention to the distance between the wire and the extractor. This distance is critical: it must be large enough to prevent any risk of impact or the formation of liquid bridges, which could disrupt the operation. However, if the distance is too great, it may become challenging to distinguish between the different tips of the emitter, which is essential for the current work. The objective of this work is to analyze as precisely as possible the contribution of each individual cone within the thruster, making it crucial to find a balance that allows for accurate differentiation while avoiding operational issues. The wire used is extremely thin, this allows the results to be as precise as possible. It has a width of 0.025 mm and is made of Tungsten.

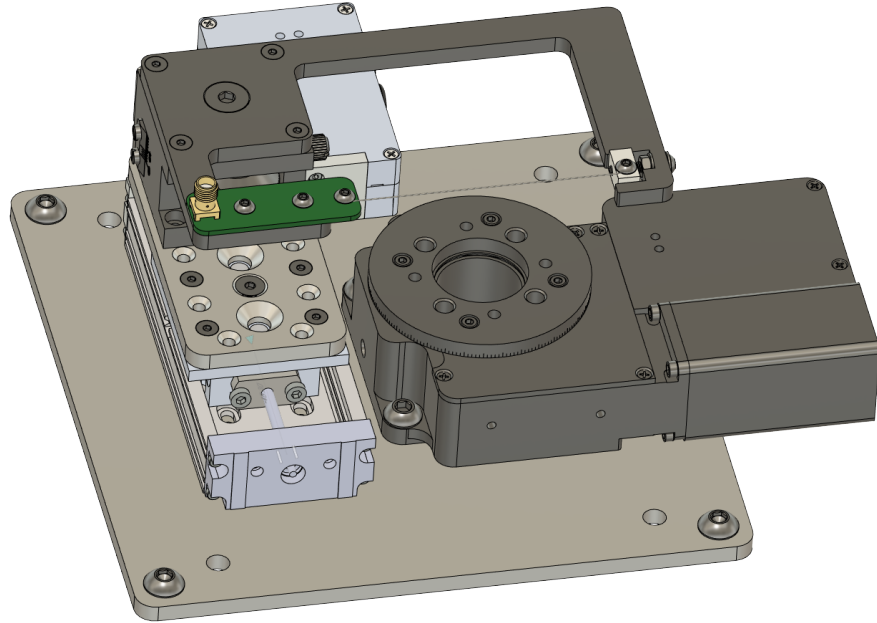


Figure 3.7: Set-up for tomography

The tomography set-up is then placed in the center of a cubic vacuum chamber (Luna) located in the clean room of ienai SPACE facilities. A turbo-molecular pump is used to keep the vacuum chamber at a pressure of 10^{-5} mbar. The latter works with an axial-flow turbine that compresses the air inside the chamber by leading the gas in the same direction as the pumping. [23] The tests are performed at ambient temperature.

The thruster operates by applying a voltage to the ionic liquid (IL) that extends to the emitter, while the extractor grid is connected to ground, which in this case corresponds to the entire vacuum chamber. It is important to keep in mind that when applying the same amplitude to both negative and positive polarities, a difference in magnitude is always observed, the negative current being slightly lower than the positive. Considering this situation, the thruster uses a square wave voltage with a different time for the polarities, this will reduce the chance of charge accumulation over time. However, this is not a perfect square voltage, as the change of polarity is not instantaneous, there is a small delay between each switch, resulting in a trapezoidal waveform. The values of the current found during those intermediate periods are hence unusable in the analysis of the data. Naturally, they result in noise, unwanted data.

3.3 ARTEMIS

To collect the data necessary for the reconstruction the emitted current, a specialized code was developed and implemented within the ARTEMIS software platform. ARTEMIS, a Python-based framework developed by ienai SPACE, facilitates the control of various instruments involved in their experiments, including the operation of the electrospray thruster.

During this thesis, a custom module was created within ARTEMIS to handle the tomography process. This code manages the precise positioning of the stages involved in the tomography setup. It provides detailed instructions that guide the stages through their required motions, ensuring that the current is collected with optimal efficiency and accuracy. This tailored approach is crucial for achieving high-quality data necessary for accurate reconstruction of the emission profile.

The first step is to differentiate the two possible operation modes. The first one being the linear stage moving at a predefined velocity as the rotary stage waits while staying motionless to receive notification to move to the next position. The second mode works the other way around: the linear stage stays fixed on a specific position during the circular motion of the rotary stage that allows current collection.

The velocity of each stage during sweeps is determined by the duration of a complete thruster cycle. Specifically, the sweeping velocity is calculated by dividing the distance traveled by the time it takes to complete the sweep. The objective is to ensure that only positive or negative emissions occur during a single sweep, simplifying the post-processing of data analysis.

Another important factor to consider is the number of cycles desired. Given that the thruster continuously emits, variations in emission over time may occur, potentially leading to inaccurate results if data from different time points are combined, especially if they stem from varying emission profiles. To achieve the most accurate results, it's crucial to analyze data collected within small, consistent time intervals.

While evaluating the time evolution of the emission is also important, it is not assessed in this thesis.

The code is divided into front-end and back-end, this allows to write a general program to which the parameters can be added according to the specific properties of the test, including the number of cycles, the method for the motions or the number of points to stop along the length of thruster. The specifics for the thruster, such as the voltage, change periodically to allow the analysis of the variation of the emission as a function of the emitted voltage.

An array is created to record the positions that will be visited while one parameter remains constant during the continuous motion of the other. Essentially, this process involves one stage performing discrete steps while the other executes sweeping motions. This approach allows for effective tracking of the procedure's state. By using the recorded positions of the wire and the collected current, the emission sites can be reconstructed using the Radon Transform. This technique, as discussed in CHAPTER 2, will be further detailed and adapted to the present case in the following chapter.

It is important to note that the shape of the emission voltage is not a perfect square wave; it does not transition instantly between negative and positive values. Instead, the focus is on the portions of the voltage that reach maximum and minimum values. Therefore, the code must account for these voltage characteristics, as the goal is to perform a complete sweep of the thruster while maintaining a constant polarity. This approach means that a full emission cycle will consist of two sweeps: one in each direction.

ANALYSIS METHODOLOGY

Computed tomography (CT) is primarily used in medical imaging and relies on reconstructing an object from a series of slices. These slices are obtained by emitting X-ray beams from one side of the object and detecting them on the opposite side.

Two measurements are taken: one of the initial emission and another at the detector placed on the other side of the object, allowing the calculation of intensity changes. These variations reflect the internal density of the object being analyzed. By performing these measurements at different angles, information about the object's internal structure can be gathered.

This data is then represented in a sinogram, a graphical depiction where each point corresponds to an intensity change for a specific angle and distance from which the X-ray is emitted. CT scanners use correction algorithms to eliminate unwanted effects, such as refracted particles, to produce a clearer image. This process was discussed in further detail in SECTION 2.2.

The methodology applied here is relatively similar, with the main difference being that no X-rays are necessary as the object is the source and the wire acts as the detector. This implies that the data of interest is an intensity instead of a variation.

Once the raw data, consisting of current measurements for various configurations, has been collected, the next step is to translate it into a visual representation of the emission sites. This chapter details the process followed to accomplish that goal.

4.1 Filtered backprojection

The Radon Transform is crucial for tomography computation as it enables the determination of the total density of a function along a specific line. In this context, the function of interest is the current along the wire.

The computation of the Radon Transform involves integrating the current density, multiplied by the width of the wire, along the length of the wire. This process provides a comprehensive representation of the current distribution, which is fundamental for accurate tomography.

Its expression is given by EQUATION 4.1, where r is the radial distance or the wire position, ϕ the angle of the wire, $j(x, y)$ the current density, W the width of the wire, and L the length of the wire. It is very similar to what was explained previously with EQUATION 2.24.

$$I(r, \phi) = \int_L j(x, y) W dl \quad (4.1)$$

However, since the data obtained with the testing is a current, it is required to transform the latter into a density. This process is executed as follows;

$$j(x, y) \approx \frac{\pi}{W N_\phi} \sum_{i=1}^{N_\phi} p_\phi(r_{px}) \quad (4.2)$$

with

$$p_\phi(r_{px}) \approx \sum_{N_r} p_\phi(r) \text{tri}\left(\frac{r_{px} - r(n)}{\Delta r}\right), \quad (4.3)$$

where

$$\text{tri}(x) = \begin{cases} 1 - |x|, & \text{if } |x| < 1 \\ 0, & \text{otherwise.} \end{cases}$$

The Radon transform is based on the concept that a 2D function can be represented by a finite number of line integrals. When multiple emitting sources are positioned along parallel paths, the Radon transform enables the computation of line integrals along these paths. To reconstruct an image, multiple parallel projections are captured by varying the sensor's position both linearly and angularly around the center of the image, which, in this case, corresponds to the emitted current of the thruster. [24]

The Radon transform involves the determination of the total density of a function along a specific line, which is defined by both an angle and a linear position. This method aligns directly with the experimental process, making the following analysis more intuitive. The analysis used in this thesis is based on Daniel G. Courtney, Zackary Wood and Timothy Fedkiw's work. [20]

The Radon transform of a distribution $f(x, y)$ is executed using EQUATION 4.4 [25]. Here, the Radon Transform is the process of gathering data along different linear positions and angles which provides directly a sinogram. The term "sinogram" originates from the fact that the result of the Radon transform of an off-center point yields a sinusoidal curve as

was showed in SUBSECTION 2.2.1. The inverse Radon transform can then be applied to the sinogram to reconstruct the image, allowing for the observation of the varying intensities of the emitting cones.

$$p(r, \phi) = \int f(x, y) \delta(r - x \cos(\phi) - y \sin(\phi)) dx dy \quad (4.4)$$

To achieve the best possible results, it is crucial to collect data as quickly as possible, ideally capturing the emission instantaneously. If the data collection process takes too long, variations in emission intensity over time could occur, leading to inaccurate results.

Data acquisition involves sweeping the wire linearly at fixed angles from an array of predefined angles, spaced by a fixed step size. By performing this sweeping over an angular range, a collection of vectors is obtained, which can be assembled into a matrix with current values for each unique point. Alternatively, data can be collected by sweeping the wire in a circular manner while keeping a constant linear position. Both methods yield a matrix of current intensities corresponding to specific wire probe positions relative to the thruster, with columns corresponding to linear positions and rows to angular positions. Plotting the contours of this matrix produces the previously discussed sinogram.

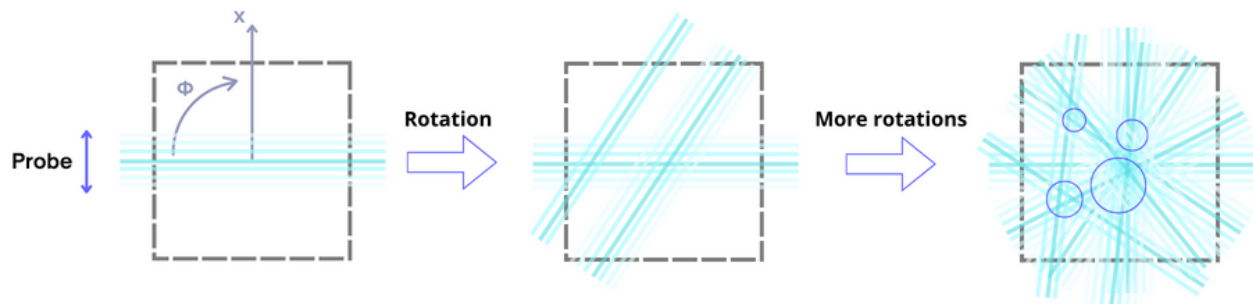


Figure 4.1: Scanning method (angular step, linear sweep)

FIGURE 4.1 shows a simplified version of how the testing method is implemented to achieve the computed tomography. This schematic shows the specific case where the angular stage moves in steps and the sweeps are linear. The thruster is represented by the dotted square and the wire serving as a probe moves following the blue lines. The probe's sweep reveals variations in intensity, highlighting differences across various regions of the emitter. This variation is expected based on the distribution of the emission. As the wire sweeps across the thruster, current accumulates in the projections due to repeated sweeps and current measurements are projected onto a Cartesian plane. This process allows the data collected by the wire to be transformed into a current map. On the resulting map, the variations of the blue color indicate different intensities of the collected current, while the purple circles highlight regions where the emission is stronger.

Once the previous step is completed, the next phase involves backprojection. [26] This is accomplished with the help of a combination between a ramp filter and the radon transform, which is how computed tomography is executed [27]. EQUATION 4.5 represents the data from the filtered sinogram found previously. Each p_Φ is a function of both r and a vector resulting from the measurements for a fixed angle Φ (for this particular method, indeed it would differ for the other one), where FFT stands for fast Fourier transform and IFFT its inverse.

However, backprojection does not give the most accurate image compared to other methods. Indeed, the resulting image is blurry. The attractiveness of this method comes from its simplicity. To compensate for this side effect, one must use a filter, which is why the combination of the two is called the filtered backprojection. The Shepp-Logan filter is used for smoothing the data. The name comes from medical imaging, where the Shepp-Logan phantom image is frequently used as an example for tomographic imaging. SUBSECTION 2.2.3 explains how this filter works.

$$p_\Phi(r) = \Delta r (IFFT[FFT[I(r, \Phi)]FFT[h(r)]] [Shepp - Logan]) \quad (4.5)$$

The ramp filter $h(t)$ is a high pass filter that stops the low frequencies with the purpose of leaving possible blurring effects out of the resulting image. The spatial interval of the latter is chosen to be the same as the linear step size, Δr .

4.2 Simulations

The CT reconstruction method was first tested numerically as part of this thesis. All simulations were carried out prior to the actual testing with the full experimental set-up and the thruster. By adjusting variables such as angular or linear resolution, wire distance, and voltage levels, expected outcomes were verified. Results were also compared using different input parameters, which was crucial for making informed decisions.

This preliminary phase was essential in guiding the experimental procedure, ensuring that the physical testing could be carried out efficiently and effectively. These simulations not only helped to anticipate potential challenges but also refined the overall procedure, contributing significantly to the reliability and success of the thruster's emission site visualization.

To accurately simulate the emission behavior of a thruster, it is crucial to consider the emission characteristics of each individual cone. This is achieved by applying a normal distribution to each cone's emission profile. Given the potential presence of non-emitting cones, a random function is utilized to determine which cones will emit and which will not.

Consequently, each simulation yields a unique emission map, as the emission characteristics vary randomly across cones.

For comparative purposes, a single emission distribution is used throughout the simulation process. This approach ensures that the results are reproducible and can be accurately compared across different scenarios, as they are derived from the same distribution. This specific emission distribution is depicted in FIGURE 4.2.

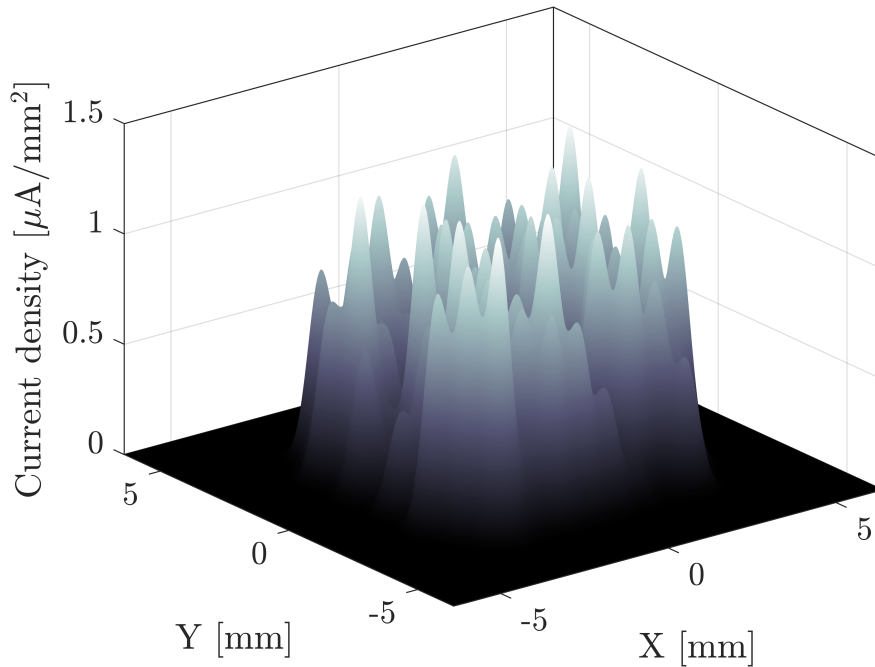


Figure 4.2: 3D distribution

The Radon transform of the emission is then applied to generate a sinogram. This sinogram represents the current intensities as a function of both linear and angular positions of the probe, visualized in a contour plot. The subsequent and most critical step is the inverse Radon transform. This step is essential for determining the resolution of the resulting current map, as it heavily depends on the number of discrete angular points used during the sinogram reconstruction. Since two methods were developed, each method involves a distinct approach to this process.

The first parameter that controls the resolution of the resulting image is the distance between the grid and the probe, z_{probe} . This distance is interdependent with the collected current. Achieving a relatively good resolution requires the wire to distinguish the contributions from each individual emission site. If it cannot, constructing a detailed image may not be possible. Indeed it makes sense that an instrument is able to rebuild only what it actually sees. This explains the need of a small distance. The relationship between the plume angle

and the wire distance is illustrated in FIGURE 4.3. However, care must be taken when positioning the wire relative to the grid. The wire should not be placed too close, as any contact with the grid could result in the wire breaking. Proper spacing is essential to prevent such issues while still accurately measuring the plume angle.

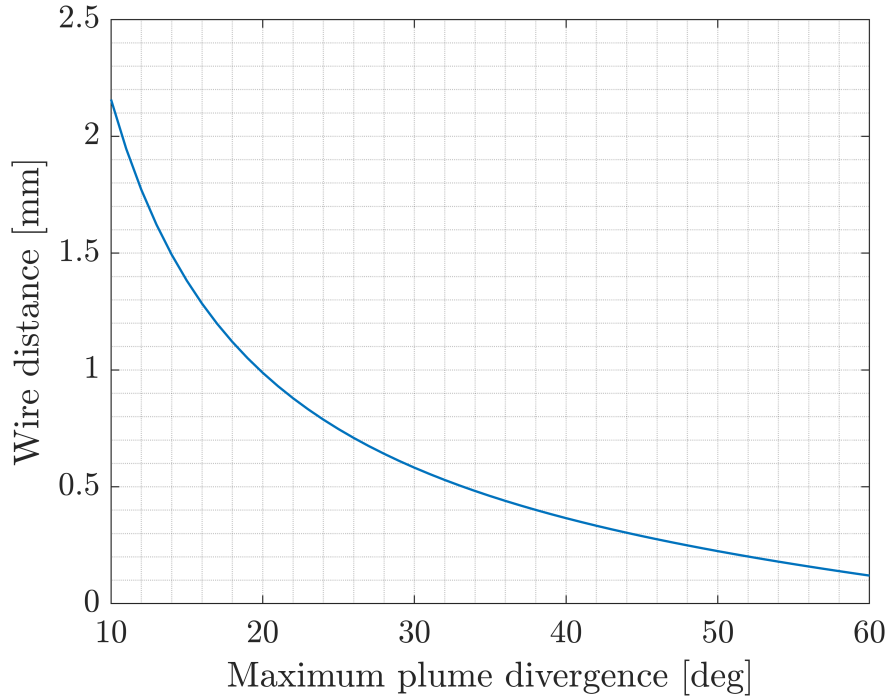


Figure 4.3: Plume divergence

FIGURE 4.4 illustrates the impact of varying the grid-wire distance, ranging from 0.2 to 1 millimeter, on the reconstructed image of the emitter. As anticipated, the quality of the reconstructed image significantly changes with this distance variation. At the smallest distance of 0.2 millimeters, the intensity of the current emitted from each individual cone is distinctly represented as well-defined dots. These dots correspond to precise emission points, allowing for a clear and detailed visualization of the emission pattern.

However, as the distance z_{probe} increases, the resolution of the reconstructed image diminishes. The previously distinct dots start to blur and merge, resulting in larger, less defined areas. This blurring effect leads to a loss of clarity, where individual cones become indistinguishable, and the emission pattern transitions into a more generalized representation. Instead of being able to pinpoint individual cones, the reconstruction now shows broader regions of emission, effectively masking the finer details of the emission sites.

This observation highlights the importance of maintaining a minimal grid-wire distance to achieve a high-resolution image that can accurately represent the emission characteristics of each cone. As the distance increases, the ability to discern individual emission sites is

compromised, resulting in a less precise and more aggregated view of the overall emission profile.

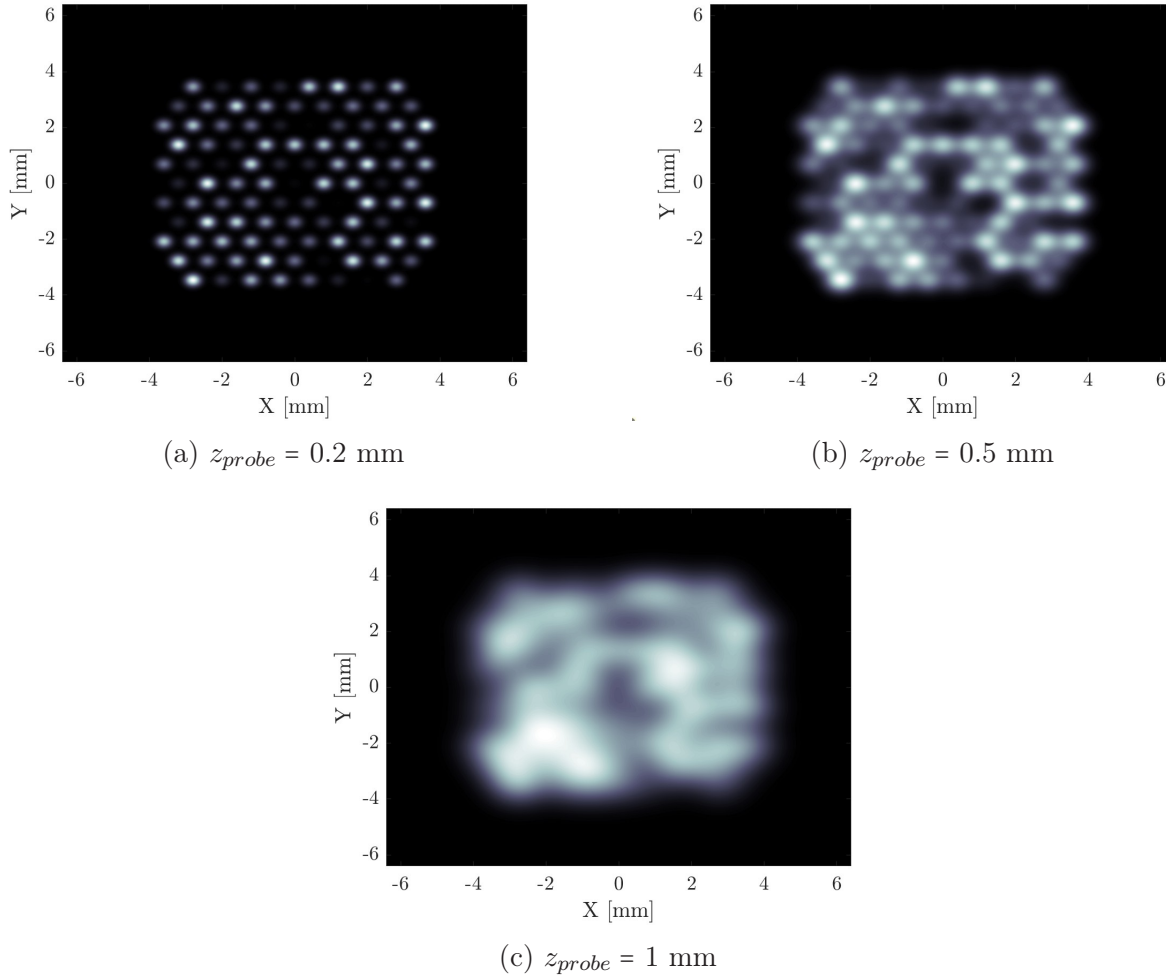


Figure 4.4: Comparison of z_{probe}

4.2.1 Angular resolution

When employing the method with angular steps, the finite set of points corresponds to discrete angular positions. This implies that the sensitivity of the angular resolution changes with the number of discrete angles used. This approach is considered the standard in tomography because applying the inverse Radon transform requires a range of angles, ideally spanning 180 degrees. To implement this method, one must define a vector of angles that aligns with the actual angular steps taken during data acquisition.

The selection of the number of angular steps is critical, as it directly affects the resolution of the reconstructed image. A higher number of steps generally leads to better resolution, but this must be balanced against the practical limitations of the experimental setup. Specif-

ically, the stage's capabilities in terms of velocity and potential heating must be taken into account. Excessive motion or overly rapid changes in position can lead to overheating, which represents a risk of permanent damage to the equipment. Thus, the choice of angular steps involves a careful compromise between achieving high-resolution imaging and maintaining the operational integrity of the stage.

The ideal scenario for accurate reconstruction involves using the maximum number of angular steps, which theoretically would be infinite. In practical terms, this translates to minimizing the step size as much as possible. The limiting factor in this process is the size of the wire. For the most precise reconstruction, the entire current emission must be captured without gaps or overlaps. Achieving this level of accuracy requires that the step size matches the width of the wire, ensuring complete and accurate data collection from each emission site.

FIGURE 4.5 illustrates the impact of varying the number of angular steps on image quality. The figure shows how the mean squared error (MSE) between the ideal reference image and the reconstructed image varies with different numbers of angular steps. The MSE is calculated using EQUATION 4.6, where n represents the number of data points, y_i denotes the actual value for the i^{th} observation, \hat{y}_i is the predicted value for the i^{th} observation, and $(y_i - \hat{y}_i)^2$ represents the squared error for the i^{th} observation. This metric quantifies the difference between the arrays representing the ideal and reconstructed images, with a lower MSE indicating a higher degree of similarity between the two images.

$$\text{MSE} = \frac{1}{n} \sum_{i=1}^n (y_i - \hat{y}_i)^2 \quad (4.6)$$

This analysis involved reconstructing a series of images, each with a different angular resolution, to evaluate how variations in the number of angles and corresponding step sizes affect the resolution and accuracy of the reconstructed images. By systematically adjusting these parameters, the impact on image quality and precision could be observed.

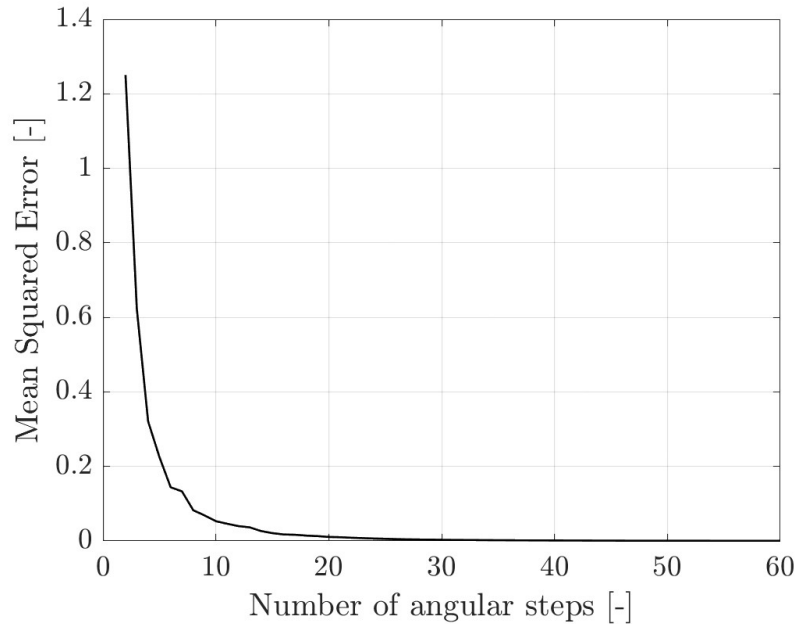


Figure 4.5: Error between the ideal case and the reconstructed image as a function of the number of angular steps

A few specific cases are plotted and discussed below to enable the selection of the optimal parameters for the actual experimentation. By analyzing these cases, one can better understand the trade-offs involved and make informed decisions that maximize the accuracy and reliability of the experimental results.

When observing the case of $z_{probe} = 0.5$ mm (FIGURE 4.6), it is evident that the resolution is directly influenced by the step size, as demonstrated in FIGURE 4.5. This correlation is logical: the smaller the step size, the greater the number of data points developed, leading to a more accurate image reconstruction and, therefore, higher image quality.

A significant improvement in quality is observed when increasing the number of steps from 10 to 35, with further enhancement from 35 to 60 steps being less pronounced. The main difference between 35 and 60 steps lies in the reduction of noise around the emission sites rather than improvements in the sites themselves. This observation aligns with the convergence graph shown in FIGURE 4.5, which indicates that after approximately 20 steps, no substantial improvements in quality should be expected.

When $z_{probe} = 1$ mm (FIGURE 4.7), it becomes apparent that the excessive distance negatively impacts the level of detail in the reconstructed image. At this increased distance, the current emitted from different cones tends to merge before reaching the wire, making challenging the distinction between individual emission sites. This merging of data results

in a loss of precision, which is evident in the last image.

Due to this loss of detail, the improvement in image quality with an increasing number of steps is less pronounced compared to cases with shorter probe distances. This suggests that as the probe moves further away from the grid, fewer steps are needed to achieve an image quality similar to what would be expected in the ideal case. In other words, the distance from the grid reduces the necessity for a high number of steps to distinguish between emission sites effectively.

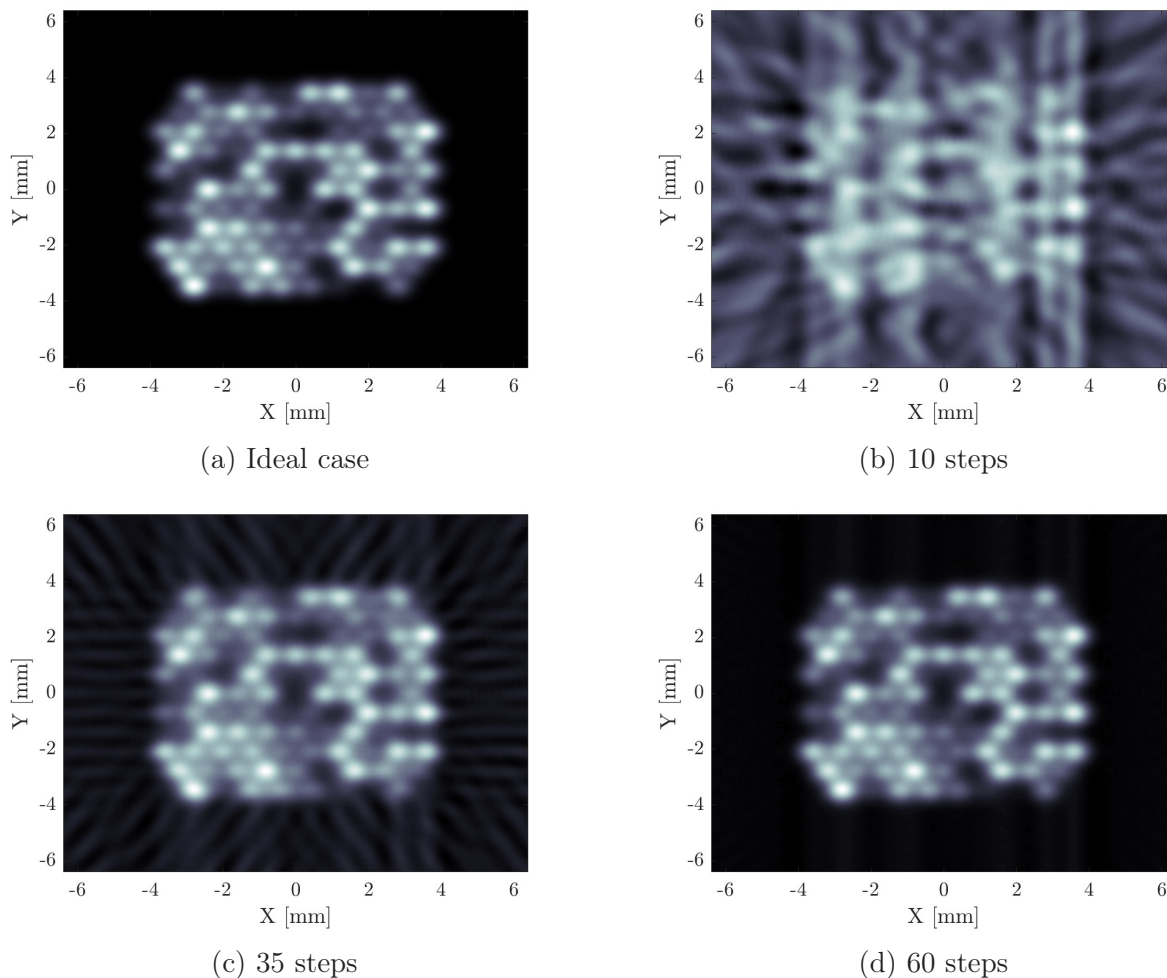


Figure 4.6: Angular steps with a $z_{probe} = 0.5$ mm

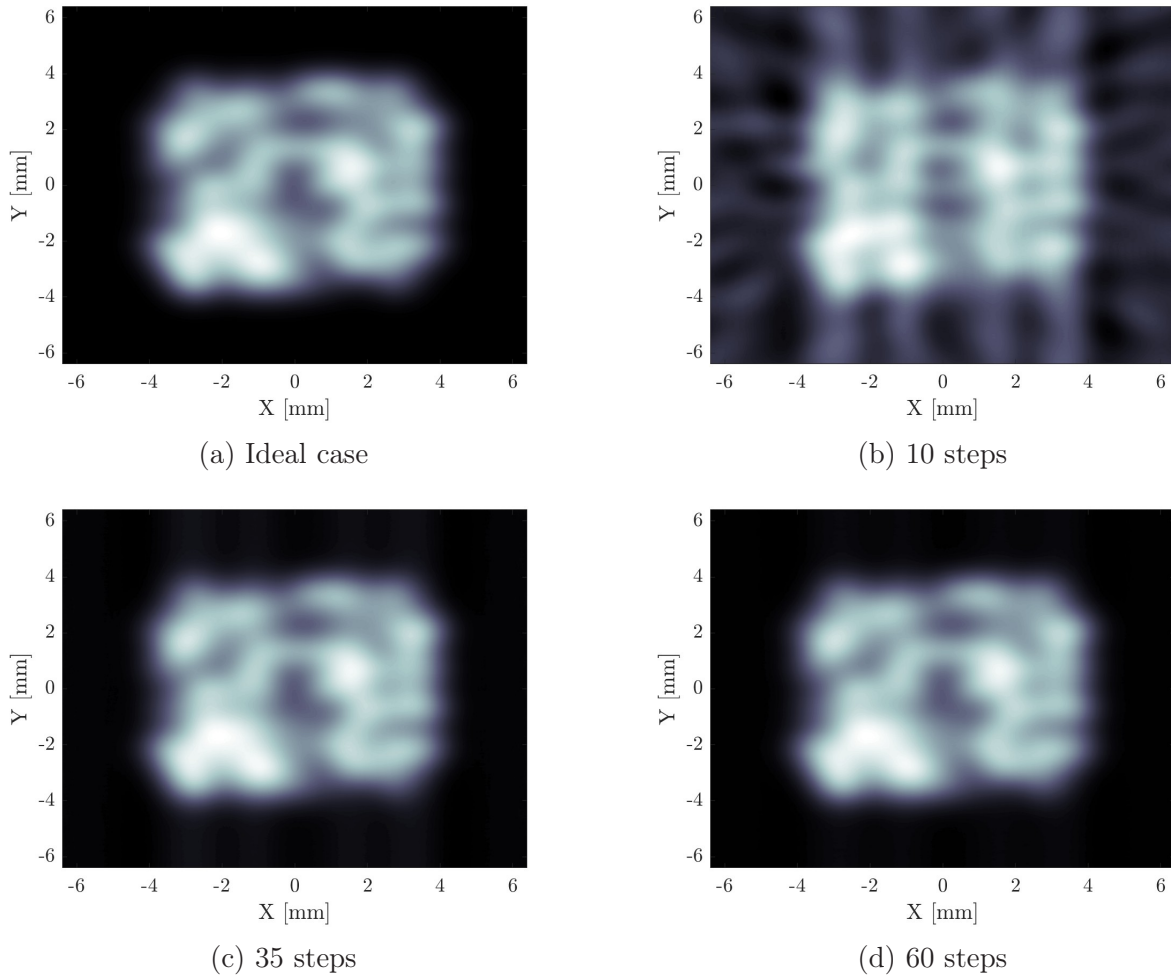


Figure 4.7: Angular steps with a $z_{probe} = 1$ mm

4.2.2 Linear resolution

For the method that utilizes linear stepping, directly inputting linear positions into the inverse Radon transform is not feasible. Therefore, an alternative approach was developed to simulate a finite number of linear steps. Since the output of the inverse Radon transform is a matrix where the lines represent linear positions and the rows correspond to angular positions, simulating a reduced number of linear steps involves selectively reducing the number of lines in this matrix.

This reduction is achieved by removing certain lines according to a pattern that aligns with the desired step size. This effectively mimics the effect of having fewer linear measurement points. Similar to the method based on angular steps, the selection of the number of steps involves finding a balance between the stage's maximum operating velocities and the risk of overheating, either from moving too quickly or too frequently, while still main-

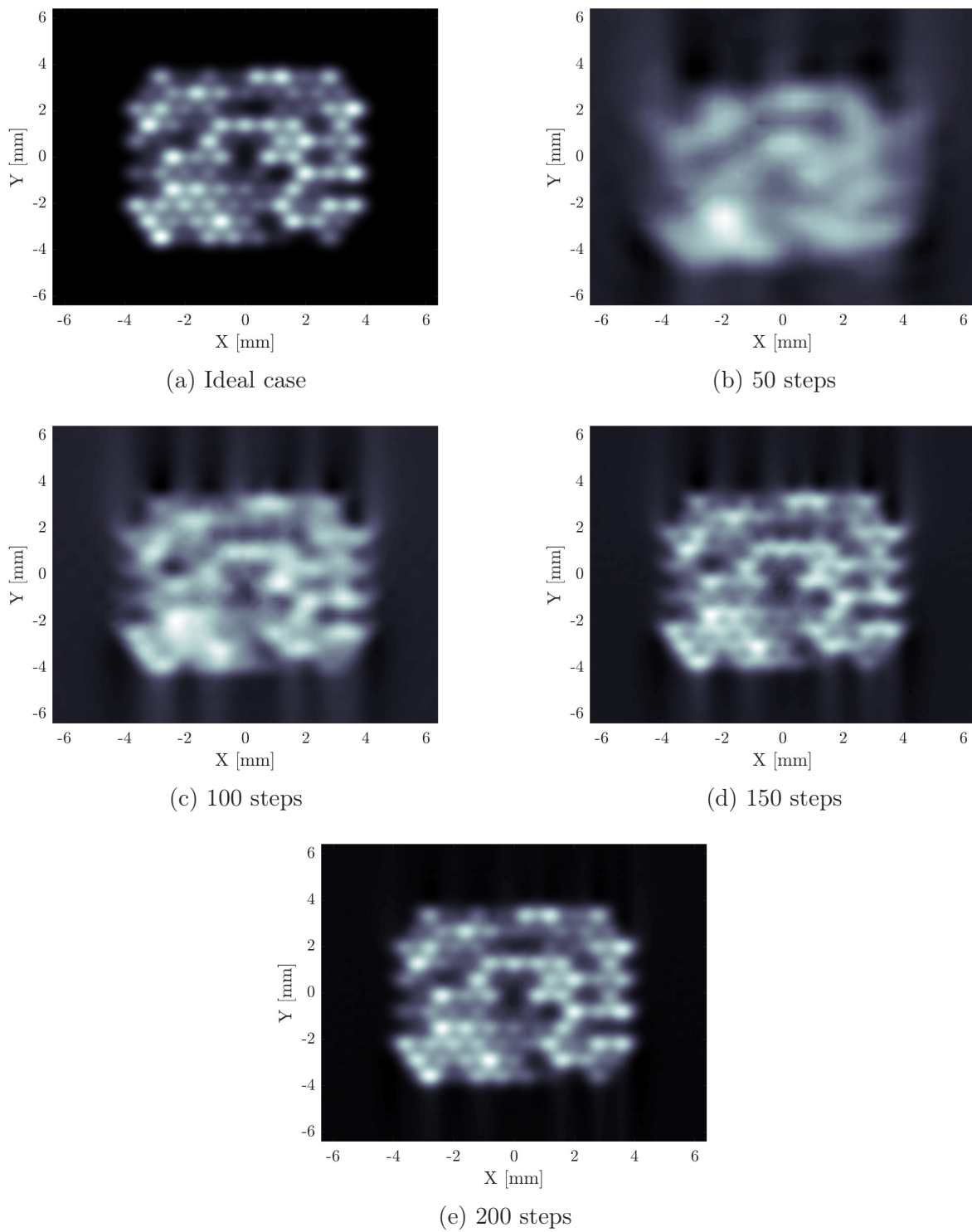
taining an acceptable resolution in the reconstructed image. This trade-off ensures that the experimental setup operates efficiently without compromising the quality of the results.

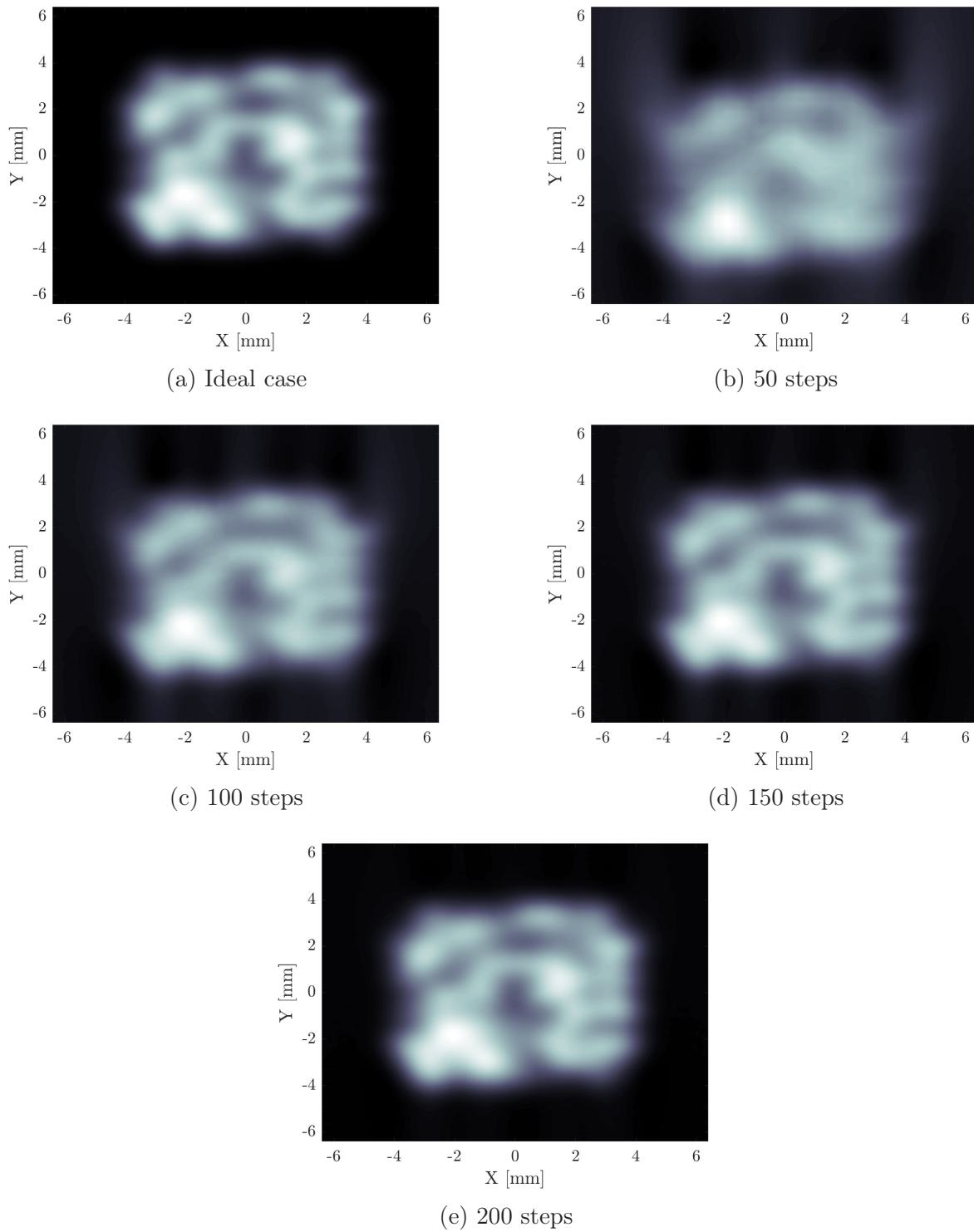
The simulation results for the second method, using different parameters, are depicted in FIGURES 4.8 and 4.9. A clear relationship between the number of steps and the resolution is evident, which aligns with expectations. While the emitting areas of the thruster are discernible even at 50 steps (FIGURE 4.8b), the emission sites are depicted as broader regions rather than distinct points corresponding to individual cones. As the number of steps increases, the clarity and distinctiveness of these emission sites improve.

A resolution with at least 150 steps is deemed acceptable, as this threshold begins to unveil clear emission sites in the images. This choice is also guided by the stage's performance capabilities. Several practical considerations must be taken into account: excessive use of the stage can lead to overheating, and as the number of steps increases, the time required to achieve full coverage also increases significantly. Balancing resolution with operational efficiency is essential for optimal performance in experimental conditions.

When analyzing the simulation results for a probe-grid distance of 1 millimeter, the primary observation is that the ideal case demonstrates a lack of distinction between the emitting sites. This blurring effect is a result of the currents merging after passing through the grid due to the distance between the cones and the probe. This outcome underscores the importance of minimizing the distance between the probe and the grid to maintain emission site resolution.

Moreover, if data is collected from a distance that is too great, the quality of the reconstruction will suffer, regardless of the number of steps taken during the process. This phenomenon is evident in FIGURE 4.9, mirroring the behavior observed in the angular stepping method. These results highlight the critical need for proximity between the probe and the grid to achieve precise and high-quality reconstructions.

Figure 4.8: Linear steps with a $z_{probe} = 0.5$ mm

Figure 4.9: Linear steps with a $z_{probe} = 1$ mm

4.2.3 Conclusion

After analyzing the simulation results, the optimal number of steps for the rotary stage is determined to be 60, while 150 steps are selected for the linear stage in their respective methods. The angular method demonstrates better performance with fewer steps, which reduces the risk of overheating. Therefore, this method is chosen for the actual experiment.

In addition to the quality of the reconstruction, the ideal wire-grid distance must also be carefully considered. The structure housing the thruster imposes certain limitations on the minimum allowable distance. Specifically, the lower limit is 0.5 mm, meaning that the wire must be positioned at a distance strictly greater than this value to avoid any risk of collision. This constraint is crucial in ensuring the safe and effective operation of the experiment.

In practice, the high number of steps initially planned for both the rotary and linear stages proved unfeasible due to overheating risks. Consequently, the resolution expectations needed to be adjusted. Instead of focusing on individual cones, which proved too challenging, the goal shifted to observing broader emission regions. This adjustment still allows for effective assessment of the thruster's performance while addressing the operational constraints.

Initial tests demonstrated that the chosen parameters led to overheating within minutes, necessitating a reassessment of the experimental setup. This required revising the image quality expectations to ensure that temperature limits were not exceeded.

Furthermore, the data rate limitations mean that each stage operates with a finite number of steps, despite the sweeping process. This practical constraint was incorporated into the simulations by adjusting the code to reflect the step limits of both stages, providing a more realistic representation of the operational conditions.

RESULTS

This chapter presents the results of testing conducted under various conditions to enable a thorough analysis. It begins with the display of sinograms from different tests, followed by the reconstructed images obtained through the inverse Radon transform. Finally, the results are discussed in detail.

The voltage waveform used for the tests is illustrated in the figure below, specifically for the 800V case. As previously described, this waveform is trapezoidal in shape.

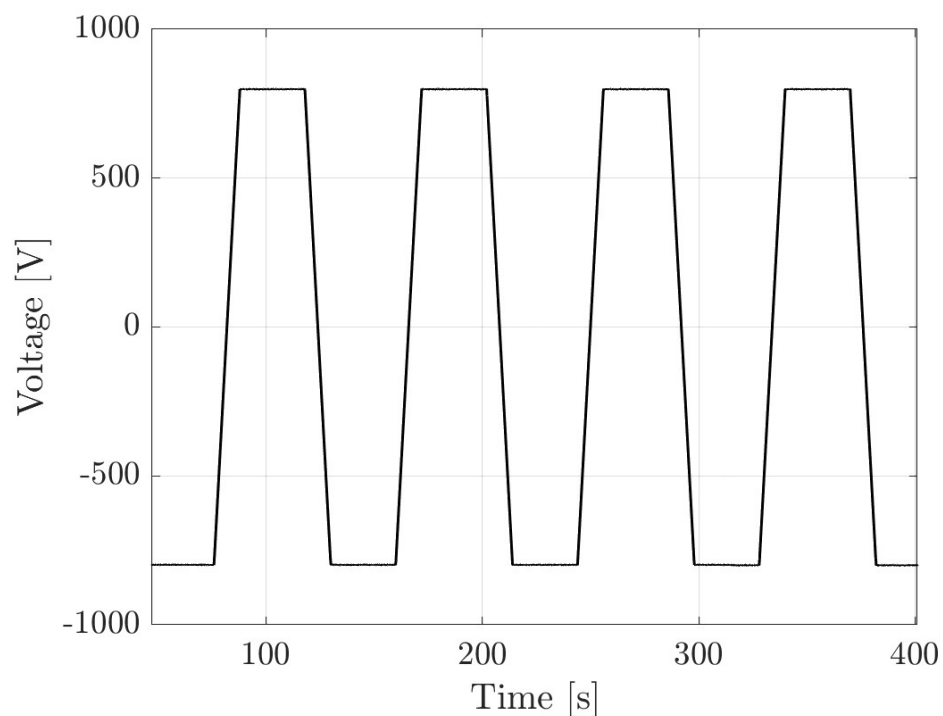


Figure 5.1: Trapezoidal voltage

5.1 Multiple emitters

As the voltage polarity changes, there is a temporary disruption and subsequent reconstruction of the Taylor cone, which introduces a small delay between the voltage and current

polarity switch. [28] This effect must be accounted for in the data post-processing. To address this, the tomography module code was designed to anticipate this delay, ensuring that the stages wait until the delay period has passed before resuming the sweep motion. This approach simplifies the analysis by ensuring that the data of interest corresponds only to the stable regions between voltage ramps.

The tests are conducted with different emitting voltages to compare and observe any effects related to voltage intensity.

The data processing is handled using a custom MATLAB code specifically designed for the purpose of this study. The code manages various data inputs, including the emitted current, voltage, time, current collected by the wire, and both linear and angular positions of the probe. It generates a sinogram from this data, where the current intensity is plotted as a function of the probe's angular and linear positions.

Before performing the inverse Radon Transform, preliminary data processing is necessary. This includes trimming the data to separate positive voltage emissions from negative ones, excluding transition voltages, and removing noise. Once the data is deemed acceptable, the inverse Radon Transform is applied to visualize the emission sites on the thruster.

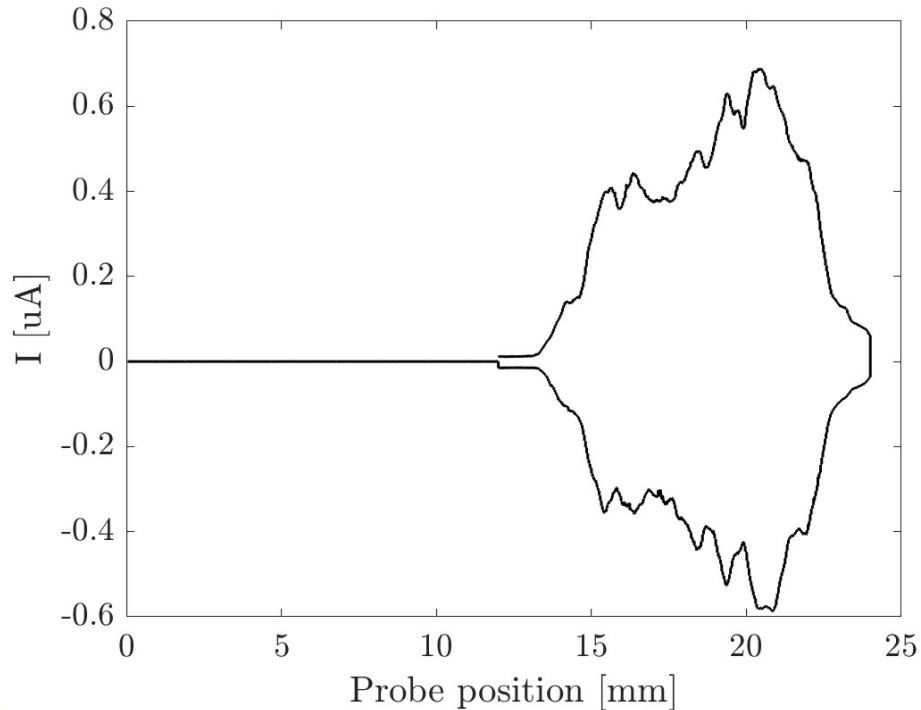


Figure 5.2: Current distribution for $\theta = 0$

FIGURE 5.2 illustrates the variation of current with the linear position at an angle of 0 degrees, indicating that the emitter's width remains constant throughout the sweeps. The

graph reveals that the highest intensity is observed near the middle length of the thruster. This result aligns with expectations, as prior analysis suggested that the outer cones of the emitter may not perform as effectively as the central ones. This initial testing campaign supports the hypothesis that the central cones are functioning better. If all the cones were performing optimally, the graph would exhibit separated peaks with comparable intensities.

For angles that are not multiples of 90 degrees, the thruster becomes misaligned with the axis of the sweep. This misalignment results in a fluctuating number of cones encountered during the sweep, peaking at the midpoint of the trajectory. This fluctuation explains the observed variation in intensity. When the wire is positioned close to the thruster, distinct peaks are visible due to the increased number of cones being sampled. Conversely, if the wire is positioned further away, the intensity profile tends to follow a Gaussian distribution, reflecting a more averaged measurement across the emission profile.

5.1.1 Sinogram

Using the matrix filled with current data, as per EQUATION 4.1, and the corresponding coordinates (i.e., the angular and linear positions), sinograms were generated for different voltages (FIGURES 5.3a to 5.3d). To produce a clear sinogram, it is crucial to collect a substantial amount of data. Without sufficient data, the sinogram can become blurry and lack detail. This underscores the importance of selecting an appropriate number of step points, which determines the size of the steps and thus the resolution of both the sinogram and the reconstructed image. This is why developing a simulation code to test various scenarios in advance was essential. The simulation code not only helped in optimizing the data collection process but also validated the technique employed.

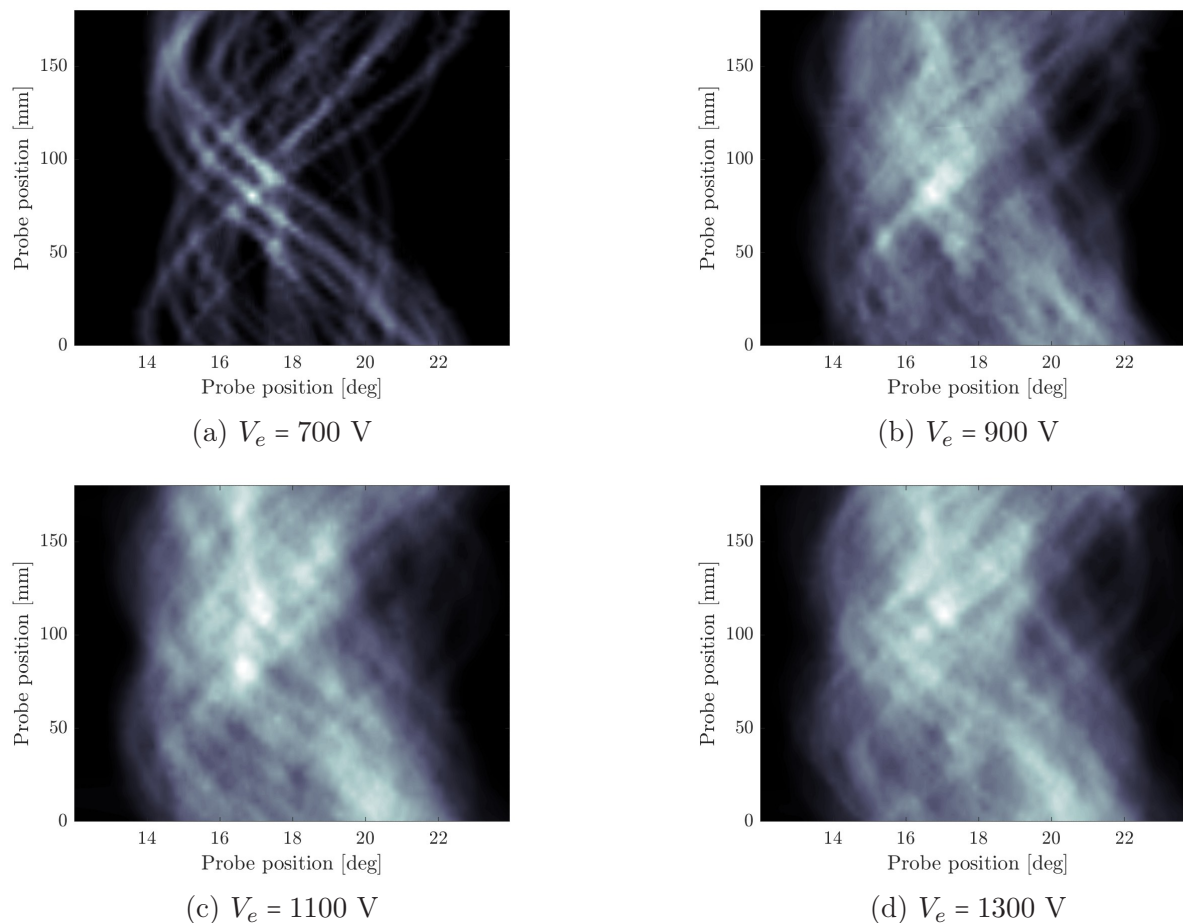


Figure 5.3: Sinograms

A sinogram can be viewed as a discrete approximation of the Radon transform. To effectively analyze this data, a backprojection is necessary, which will be detailed in the following section.

As discussed in SECTION 2.2.1, the Radon transform of a point source yields a sinusoid. Observing FIGURES 5.3a to 5.3d, it is evident that as the voltage increases, the number of sinusoids apparent on the graph also increases. This signifies that more data points are available, which enhances the clarity of the results. Specifically, while the quantity of sinusoidal patterns changes with the voltage, the information about the intensity remains consistent. This is due to the fact that a single thruster was used throughout the testing campaign, ensuring that variations in the results are attributed to the voltage changes rather than differences in the thruster itself.

5.1.2 Backprojection

Now that the sinograms have been reconstructed, the next and final step is to reconstruct the intensity map. This is achieved using the backprojection method, which relies on the mathematical principles of the Radon transform.

The backprojection process allows for an accurate visual representation of the emission sites, providing detailed insight into the distribution and intensity of the emitted currents. This step is crucial for assessing and analyzing the performance of the thruster based on the reconstructed intensity map.

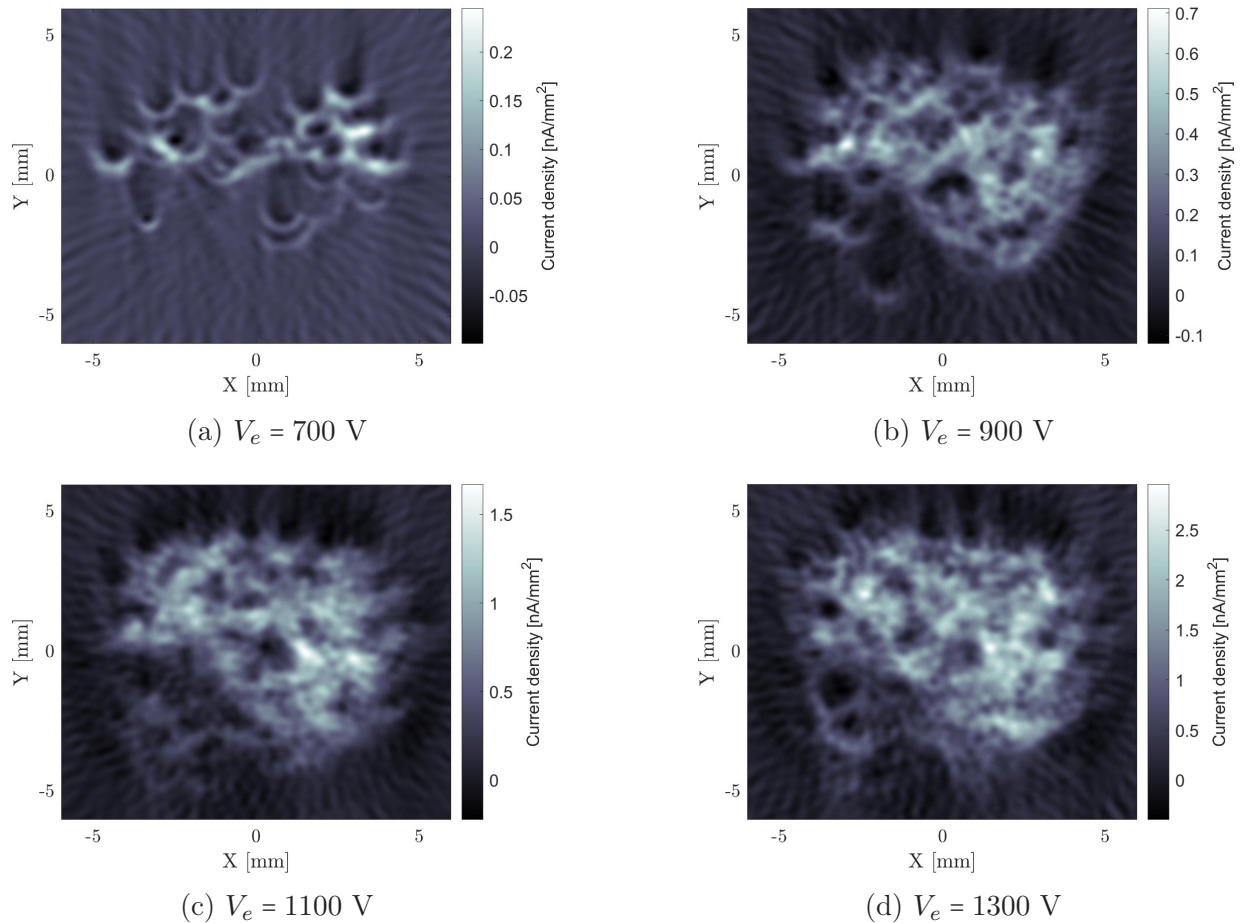


Figure 5.4: Intensity maps

In FIGURE 5.4, the variation in emissions as a function of the thruster's applied voltage is illustrated. The experimental results closely align with the predictions made during simulations, confirming the accuracy of the models used. As the voltage increases, the emission spots become more defined, offering a clearer understanding of the emission pattern. This improved clarity at higher voltages highlights the correlation between applied voltage and

emission site visibility, further validating the simulation's predictive capability.

5.2 Discussion

The emission site remains consistent across different voltage settings, revealing a clear correlation where the lower left portion of the thruster exhibits reduced emission compared to the rest of the device. As the voltage increases, the overall image quality and intensity improve, reflecting a higher current density.

The results align well with the predictions from the simulations, which provided sufficient information to optimize parameters such as the wire-to-grid distance. This careful parameter selection contributed to the accuracy of the results.

However, these results reveal that the thruster must have some anomalies. Specifically, a consistent lack of emission in a specific region of the thruster, regardless of the voltage applied. This suggests potential manufacturing issues. These issues could stem from imperfections in the cone texturization that prevent the propellant from adequately rising or from the tips not being sufficiently pointed.

Another possible explanation involves the feeding holes, which might have been obstructed, or misalignment between the tank and the emitter. Such misalignment could result in uneven propellant distribution across the emitter, leading to reduced particle ejection in the affected area. This uneven distribution could account for the observed decrease in emission in that specific region.

This issue could also be attributed to variations in the electric field distribution, which may arise from several sources. Non-uniformities in the extractor grid, such as irregularities in hole sizes or misalignment, can lead to inconsistent electric field strength across the emitter array. Similarly, imperfections or variations in the emitter geometry, such as deviations in cone shape or spacing, can disrupt the uniformity of the field. These discrepancies in the electric field can cause uneven emission profiles, resulting in some areas of the thruster emitting more or less than others. Addressing these issues typically involves improving the precision in the design and manufacturing of both the extractor grid and emitter components to ensure a more consistent electric field and uniform emission.

CONCLUSION

The objective of this thesis was to use computed tomography to reconstruct the current emission of an electrospray thruster.

An initial review of what the current body of literature enabled to understand the functioning of an electrospray thruster and computed tomography. The former is the acceleration of ionic particles, coming from the propellant used, with an electric field that will initially form a Taylor cone before the ions are able to leave the emitter. The latter is based on the Radon transform which is a mathematical tool that allows the reconstruction of the emission site based on the values of the current being captured with a wire that is being swept across the thruster. This method is inspired by CT scanners used for imaging in the medicine domain.

To achieve this, the procedure for testing in the vacuum chamber had to be meticulously planned. The process began with simulations to determine the necessary parameters for efficient testing and to set realistic expectations for the results. Following the simulations, the ARTEMIS platform developed by ienai SPACE was used, although it required customization. ARTEMIS, which already had modules for the various instruments used by ienai SPACE, needed an additional module to accommodate the CT. This new module was specifically designed during this thesis to manage the thruster's movements, ensuring comprehensive coverage. Given that the thruster could only be moved using motion stages, the module was developed to control both the linear and rotary stages essential for this purpose.

Once the previous phase was completed, the actual testing could be performed, enabling the acquisition of results. The setup featured ienai SPACE's ATHENA thruster, which includes an emitter with one hundred and one cones and an extractor crucial for generating the extracting electric field. The computed tomography was facilitated by the assembly of a collecting wire and two stages that enabled its precise motion.

Finally, the comparison between the actual results and the simulations done beforehand was made and one could make the observation that the simulations were a good representation of reality. Additionally, the data showed that as the voltage increases, the distribution becomes more homogeneous.

The results indicate that the thruster was not operating at full capacity, which aligns with the expectation of possible manufacturing imperfections. Specifically, the lower left corner of the thruster exhibited consistently lower emission levels across all tested voltages. This pattern suggests a possible manufacturing defect, although further investigation of the thruster is needed to confirm this and understand the underlying issue. The method developed in this study is valuable for identifying such discrepancies, allowing for a targeted investigation into possible causes of the imperfection.

These findings have the potential to significantly advance the understanding of electro-spray thrusters. By identifying areas of imperfection and assessing performance inconsistencies, this research can inform future design and manufacturing processes. Consequently, it could lead to more efficient and reliable space propulsion systems, improving both the effectiveness and dependability of thrusters in space missions.

PROPERTIES OF THE RADON TRANSFORM

A.1 Linearity

Following the definition of the Radon transform, the linearity is defined, with g_q functions and α_q an array of constants.

$$g(x, y) = \sum_q \alpha_q g_q(x, y) \quad \Rightarrow \quad \tilde{g}(\rho, \theta) = \sum_q \alpha_q \tilde{g}_q(\rho, \theta) \quad (\text{A.1})$$

A.2 Symmetry

The Radon transform is symmetric and obeys the following law

$$\tilde{g}(\rho, \theta) = \tilde{g}(-\rho, \theta + \pi). \quad (\text{A.2})$$

A.3 Scaling

By choosing a and b positive constants, and scaling the variables as follows

$$h(x, y) = g\left(\frac{x}{a}, \frac{y}{b}\right), \quad (\text{A.3})$$

one can compute the Radon transform,

$$\begin{aligned} \tilde{h}(\rho, \theta) &= \int_{-\infty}^{\infty} \int_{-\infty}^{\infty} g\left(\frac{x}{a}, \frac{y}{b}\right) \delta(\rho - x \cos \theta - y \sin \theta) dx dy \\ &= ab \int_{-\infty}^{\infty} \int_{-\infty}^{\infty} g(\tilde{x}, \tilde{y}) \delta(\rho - a\tilde{x} \cos \theta - b\tilde{y} \sin \theta) d\tilde{x} d\tilde{y} \\ &= \frac{ab}{|\gamma|} \int_{-\infty}^{\infty} \int_{-\infty}^{\infty} g(\tilde{x}, \tilde{y}) \delta\left(\frac{\rho}{\gamma} - \tilde{x} \frac{a \cos \theta}{\gamma} - \tilde{y} \frac{b \sin \theta}{\gamma}\right) d\tilde{x} d\tilde{y} \\ &= \frac{ab}{|\gamma|} \int_{-\infty}^{\infty} g(\tilde{x}, \tilde{y}) \delta(\tilde{\rho} - \tilde{x} \cos \tilde{\theta} - \tilde{y} \sin \tilde{\theta}) d\tilde{x} d\tilde{y} \\ &= \frac{ab}{|\gamma|} \tilde{g}(\tilde{\rho}, \tilde{\theta}) \end{aligned}$$

where

$$\cos\tilde{\theta} = \frac{a\cos\theta}{\gamma} \quad \& \quad \sin\tilde{\theta} = \frac{b\sin\theta}{\gamma} \quad (\text{A.4})$$

$$\tilde{x} = \frac{x}{a} \quad \& \quad \tilde{y} = \frac{y}{b} \quad (\text{A.5})$$

Out of which, one must normalize the squared sums, as follows

$$\cos^2\tilde{\theta} + \sin^2\tilde{\theta} = 1 \quad \Rightarrow \quad a^2\cos^2\theta + b^2\sin^2\theta = \gamma^2. \quad (\text{A.6})$$

Additionally, from EQUATIONS A.4 γ can be expressed as

$$\frac{a\cos\theta}{\cos\tilde{\theta}} = \gamma = \frac{b\sin\theta}{\sin\tilde{\theta}}, \quad (\text{A.7})$$

leading to having

$$\tan^{-1}\left(\frac{a}{b}\tan\theta\right) = \tilde{\theta} \quad \& \quad \tilde{\rho} = \frac{\rho}{\gamma} = \frac{\rho}{\sqrt{a^2\cos^2\theta + b^2\sin^2\theta}}. \quad (\text{A.8})$$

A.4 Shifting

The function h is a shifted version of g ,

$$h(x, y) = g(x - x_0, y - y_0). \quad (\text{A.9})$$

The Resulting Radon transform is thus

$$\begin{aligned} \tilde{h}(\rho, \theta) &= \int_{-\infty}^{\infty} \int_{-\infty}^{\infty} g(x - x_0, y - y_0) \delta(\rho - x\cos\theta - y\sin\theta) dx dy \\ &= \int_{-\infty}^{\infty} \int_{-\infty}^{\infty} g(\tilde{x}, \tilde{y}) \delta((\rho - x_0\cos\theta - y_0\sin\theta) - \tilde{x}\cos\theta - \tilde{y}\sin\theta) d\tilde{x} d\tilde{y} \\ &= \tilde{g}(\rho - x_0\cos\theta - y_0\sin\theta, \theta). \end{aligned}$$

A.5 Rotation

In order to make the rotation as simple as possible, the coordinates are changed into polar form,

$$h(r, \phi) = g(r, \phi - \phi_0). \quad (\text{A.10})$$

One can then compute the Radon transform of the h function

$$\begin{aligned}
\tilde{h}(\rho, \theta) &= \int_{-\infty}^{\infty} \int_0^{\pi} g(r, \phi - \phi_0) \delta(\rho - r \cos \phi \cos \theta - r \sin \phi \sin \theta) d\phi dr \\
&= \int_{-\infty}^{\infty} \int_0^{\pi} g(r, \tilde{\phi}) \delta(\rho - r \cos(\theta - \tilde{\phi} - \phi_0)) |r| d\tilde{\phi} dr \\
&= \tilde{g}(\rho, \theta - \phi_0)
\end{aligned}$$

A.6 Convolution

Starting by taking two functions $f(x, y)$ and $g(x, y)$ and generating the function $h(x, y)$ as the 2D convolution out of the two of them

$$h(x, y) = f(x, y) \star^x \star^y g(x, y) = \int_{-\infty}^{\infty} \int_{-\infty}^{\infty} f(x_1, y_1) g(x - x_1, y - y_1) dx_1 dy_1. \quad (\text{A.11})$$

The Radon transform can be evaluated as follows

$$\begin{aligned}
\tilde{h}(\rho, \theta) &= \int_{-\infty}^{\infty} \int_{-\infty}^{\infty} \int_{-\infty}^{\infty} \int_{-\infty}^{\infty} f(x_1, y_1) g(x - x_1, y - y_1) \delta(\rho - x \cos \theta - y \sin \theta) dx_1 dy_1 dx dy \\
&= \int_{-\infty}^{\infty} \int_{-\infty}^{\infty} f(x_1, y_1) \int_{-\infty}^{\infty} \int_{-\infty}^{\infty} g(x - x_1, y - y_1) \delta(\rho - x \cos \theta - y \sin \theta) dx dy dx_1 dy_1 \\
&= \int_{-\infty}^{\infty} \int_{-\infty}^{\infty} f(x_1, y_1) \tilde{g}(\rho - x_1 \cos \theta - y_1 \sin \theta, \theta) dx_1 dy_1 \\
&= \int_{-\infty}^{\infty} \int_{-\infty}^{\infty} f(x_1, y_1) \int_{-\infty}^{\infty} \tilde{g}(\rho - \rho_1, \theta) \delta(\rho_1 - x_1 \cos \theta - y_1 \sin \theta, \theta) d\rho_1 dx_1 dy_1 \\
&= \int_{-\infty}^{\infty} \tilde{g}(\rho - \rho_1, \theta) \int_{-\infty}^{\infty} \int_{-\infty}^{\infty} f(x_1, y_1) \delta(\rho_1 - x_1 \cos \theta - y_1 \sin \theta, \theta) dx_1 dy_1 d\rho_1 \\
&= \int_{-\infty}^{\infty} \tilde{f}(\rho_1, \theta) \tilde{g}(\rho - \rho_1, \theta) d\rho_1 \\
&= \tilde{f}(\rho, \theta) \star^{\rho} \tilde{g}(\rho, \theta)
\end{aligned}$$

One can conclude that the Radon transform of a two dimensional convolution results in a one dimensional convolution of the Radon transform of each individual function. [29]

DELTA DIRAC FUNCTION

The Delta Dirac function, also known as the impulse symbol [30], δ , is a generalized function. The basic definition is

$$\delta(x) = 0 \quad \text{for } x \neq 0 \quad (\text{B.1})$$

$$\int_{-\infty}^{\infty} \delta(x) dx = 1, \quad (\text{B.2})$$

and interesting properties of the latter are

$$\int_{-\infty}^{\infty} g(x)(ax + b) dx = \frac{1}{|a|} \int_{-\infty}^{\infty} g\left(\frac{x-b}{a}\right) \delta(x) dx = \frac{1}{|a|} g\left(\frac{-b}{a}\right), \quad (\text{B.3})$$

$$\int_{-\infty}^{\infty} f(x) \delta(x-a) dx = f(a), \quad (\text{B.4})$$

$$\int_{a-\epsilon}^{a+\epsilon} f(x) \delta(x-a) dx = f(a) \quad \text{with } \epsilon > 0, \quad (\text{B.5})$$

$$\delta(ax) = \frac{1}{|a|} \delta(x) \quad \text{with } x \neq a. \quad (\text{B.6})$$

The function can be written under the following form

$$\delta(g(x)) = \sum_i \frac{\delta(x-x_i)}{|g'(x_i)|} \quad (\text{B.7})$$

with x_i the roots of the function g , which allows to find that

$$\int_{-\infty}^{\infty} g(x) \delta(f(x)) dx = \sum_{i=1}^I \frac{g(x_i)}{|f'(x_i)|}. \quad (\text{B.8})$$

BIBLIOGRAPHY

- [1] Ataman C. Ryan C. N. Chakraborty S. Courtney D. G. Stark J. P. W. Dandavino, S. and H Shea. Microfabricated electrospray emitter arrays with integrated extractor and accelerator electrodes for the propulsion of small spacecraft. *Journal of Micromechanics and Microengineering*, 24(7), 2014.
- [2] Peter Tolf. The radon transform - theory and implementation. 1996.
- [3] Antonis Vamvakeros. Operando chemical tomography of packed bed and membrane reactors for methane processing. 2017.
- [4] Anil K. Jain. *Fundamentals of Digital Image Processing*. Thomas kailath edition, 1989.
- [5] Charles N Ryan Chengyu Ma. The design and characterization of a porous-emitter electrospray thruster (pet-100) for interplanetary cubesats. 2018.
- [6] Kristina M. Lemmer Jonathan Kolbeck Michael Keidar Hiroyuki Koizumi Han Liang Daren Yu Tony Schönherr Jose Gonzalez del Amo Wonho Choe Riccardo Albertoni Andrew Hoskins Shen Yan William Hart Richard R. Hofer Ikkoh Funaki Alexander Lovtsov Kurt Polzin Anton Olshanskii Dan Lev, Roger M. Myers and Olivier Duchemin. The technological and commercial expansion of electric propulsion in the past 24 years. 2017.
- [7] Mick Wijnen Sara Correyero Pablo Fajardo David Villegas-Prados, Javier Cruz and Jaume Navarro-Cavallé. Impact of propellant temperature on the emission regime of an externally wetted electrospray system using time-of-flight mass spectrometry. *Elsevier*, 308(213):145–155, 2023.
- [8] Paulo C. Lozano. Studies on the ion-droplet mixed regime in colloid thrusters. 2003.
- [9] Jen Beatty. The radon transform and the mathematics of medical imaging. *Colby*, 646, 2012.
- [10] ESA. Athena thruster kicks off electrospray propulsion for nanosatellites, 2023-03-10. https://www.esa.int/Enabling_Support/Space_Engineering_Technology/Shaping_the_Future/ATHENA_thruster_kicks_off_electrospray_propulsion_for_NanoSatellites.
- [11] Chase Coffman. Electrically-assisted evaporation of charged fluids: Fundamental modeling and studies on ionic liquids. 2016.
- [12] Marco Rostello. Preliminary sizing of an electrospray thruster. 2017.

- [13] Qi Kang Senwen Xue, Li Duan. Fabrication of externally wetted emitter for ionic liquid electro spray thruster by low-speed wire cutting combined with electrochemical etching. 2021.
- [14] Georg Herdrich Dillon O'Reilly and Darren F. Kavanagh. Electric propulsion methods for small satellites: A review. *Aerospace*, 8(22), 2021.
- [15] Robert S. Legge Jr. Fabrication and characterization of porous metal emitters for electro spray applications. 2006.
- [16] Akintunde Ibitayo Akinwande Blaise Gassend, Luis Fernando Velásquez-García and Manuel Martínez-Sánchez. A microfabricated planar electro spray array ionic liquid ion source with integrated extractor. *Journal of Microelectromechanical Systems*, 18(3):679–694, 2009.
- [17] L. A. Shepp and J. B. Kruskal. Computerized tomography: The new medical x-ray technology. 1978.
- [18] C. D. Rayson C. A. Monnig, K. A. Marshall and G. M. Hieftje. Tomographic image reconstruction techniques for spectroscopic sources: Theory and computer simulations. 1988.
- [19] Russ Elliott. Deflection of beams, 2010. <http://www.clag.org.uk/beam.html>.
- [20] Zackary Wood Daniel G. Courtney and Timothy Fedkiw. Reconstructing electro spray plume current spatial distributions using computed tomography. 2019.
- [21] Zaber. X-rsw60a-sv2 datasheet, 2022-07-27. <https://www.zaber.com/api/assets/X-RSW60A-SV2-Datasheet.pdf>.
- [22] Zaber. X-lsm-sv2 manual, 2024. <https://www.zaber.com/manuals/X-LSM-SV2>.
- [23] Edwards Vacuum. Turbo-molecular pumps. <https://www.edwardsvacuum.com/en-uk/our-products/turbomolecular-pumps/next-mechanical-turbomolecular-pumps>.
- [24] MatLab. Radon transform. <https://www.mathworks.com/help/images/radon-transform.html>.
- [25] The American Association of Physicists in Medicine. Tomographic image reconstruction. <https://www.aapm.org/meetings/99AM/pdf/2806-57576.pdf>.
- [26] Jun-Wei Jia Yuan-He Zhang Chen-Guang Liu Zhong-Xi Ning Da-Ren Yu Yan-Fei Wang, Xi-Ming Zhu. Development of a circumferential-scanning tomography system for the measurement of 3-d plume distribution of the spacecraft plasma thrusters. *Measurement*, 216(112966), 2023.
- [27] Jiang Hsieh Yuchuan Wei, Ge Wang. An intuitive discussion on the ideal ramp filter in computed tomography (i). *Computers and Mathematics with Applications*, (49):731–740, 2004.

- [28] Manuel Martínez-Sánchez Paulo Lozano. Ionic liquid ion sources: characterization of externally wetted emitters. *Journal of Colloid and Interface Science*, (5724):415–421, 2005.
- [29] Béla Kári. The properties of the radon transform, 2019. <http://oftankonyv.reak.bme.hu/tiki-index.php?page=The+properties+of+the+Radon+transform>.
- [30] Eric W. Weisstein. Delta function, 2024. <https://mathworld.wolfram.com/DeltaFunction.html>.